Modeling of the Dec. 22nd 2018 Anak Krakatau volcano lateral collapse and tsunami based on recent field surveys: comparison with observed tsunami impact

Grilli[1] S.T., Zhang[2] C., Kirby[2] J.T., Grilli[1] A.R., Tappin[3,4] D., Watt[5] S.F.L., Hunt[6], J.E., Novellino[3], A., Engwell[3] S., Nurshal M.E.M.[7], Abdurrachman M.[7], Cassidy, M.[8], Madden-Nadeau A.L.[8] and S. Day[4]

1. Department of Ocean Engineering, University of Rhode Island, USA
2. Center for Applied Coastal Research, University of Delaware, USA
3. British Geological Survey, Nottingham, UK
4. University College, London, UK
5. School of Geography, Earth and Environmental Sciences, University of Birmingham, UK
6. National Oceanography Centre, Southampton, UK
7. Bandung Institute of Technology, Indonesia
8. Department of Earth Sciences, University of Oxford, UK

Abstract

The Dec. 22, 2018 lateral collapse of the Anak Krakatau (AK) volcano in the Sunda Straits of Indonesia discharged volcaniclastic material into the 250 m deep caldera southwest of the volcano and generated a large tsunami, causing runups of up to 85 m in the near-field, and 13.5 m in the far-field, on the nearby coasts of Sumatra and Java. The tsunami caused at least 437 fatalities, the greatest number from a volcanically-induced tsunami since the catastrophic explosive caldera-forming eruption of Krakatau in 1883 and the sector collapse of Ritter Island in 1888. For the first time in over 100 years, the 2018 AK event provides an opportunity to study a major volcanically-generated tsunami that caused widespread loss of life and significant damage. Here, we present numerical simulations of the collapse and tsunami generation, propagation, and coastal impact, with state-of the-art numerical models, using both a new parametrization of the collapse and a

near-field bathymetric dataset based on our 2019 field surveys and satellite images. These subaerial and submarine data sets are used to constrain the geometry and magnitude of the landslide mechanism, which show that the primary landslide scar bisected the AK edifice, cutting behind the central vent and removing 50% of its subaerial volume. The primary landslide volume is estimated to range from 0.175 – 0.272 km^3, based on uncertainties in the shape of the submerged part of the failure plane. This is supported by an independent estimate of the primary deposit volume of 0.214 ± 0.036 km^3. Given uncertainties in the failure volume, and a secondary debris flow triggered by the collapse (0.022 ± 0.006 km^3), we define a range of potential failure surfaces that span these values in 4 collapse scenarios of volume ranging from 0.175 to 0.313 km^3. These AK collapses are modeled, assuming either a granular or viscous fluid rheology, together with their corresponding tsunami generation and propagation. Observations of a single tsunami, with no subsequent waves, are consistent with our interpretation of landslide failure in a rapid, single phase of movement rather than a more piecemeal process, generating a tsunami which reached nearby coastlines within ~30 minutes. Both modelled rheologies successfully reproduce near- and far-field tsunami flow depth and runup observed in all post-event field survey results, tide gauge records, and eyewitness reports to date, suggesting our estimated landslide volume range is appropriate. This event highlights the significant hazard posed by relatively small-scale lateral volcanic collapses, which can occur *en-masse*, without any precursory signals, and are an efficient and unpredictable tsunami source. Our successful simulations demonstrate that current numerical models can accurately forecast tsunami hazards from these events. In cases such as Anak Krakatau's, the absence of precursory warning signals, together with the short travel time following tsunami initiation present a major challenge for mitigating tsunami coastal impact, stressing the need to install early warning systems.

Commented [SG1]: To be reconciled with Hunt et al

1 Introduction

Over the past 20 years, catastrophic tsunamis in Papua New Guinea (1998), the Indian Ocean (2004), and Japan (2011) have led to major advances in understanding and modeling tsunamis from submarine landslides, earthquakes, and dual mechanisms. These advances have been mainly based on improved constraints on these recent events and their geographical distribution, together with improved numerical tsunami modelling capability (e.g., Tappin et al., 2008; Grilli et al., 2007; Ioualalen et al., 2007; Grilli et al., 2013; Kirby et al., 2013; Tappin et al., 2014; see Yavari-Ramshe and Ataie-Ashtiani, 2016, for a recent review). Tsunamis from volcanic eruptions and collapses, however, although having the potential for generating mega-tsunamis (Paris et al., 2020b), resulting in significant loss of life and property (Day, 2015; Paris, 2015), and accounting for 20% of all volcanic fatalities over the past 400 years (Auker et al., 2013), remain less well-studied because, up until recently, there were few well-recorded and researched events.

Most of the earlier known volcanic collapse events are prehistoric, with no recorded direct observations, and many were large-volume lateral volcanic collapses of ocean islands, such as in the Canary Islands (e.g., Ward and Day, 2001; Day et al., 2005; Løvholt et al., 2008; Abadie et al., 2012; Giachetti et al., 2012) and Hawaii (e.g. McMurty et al. 2003), although some were smaller scale events, such as Ritter Island 1988 (Ward and Day, 2003) and Stromboli 2002 (Tinti et al., 2000; Fornaciai et al., 2019). Of historical volcanic tsunamis the best studied are Krakatau, Indonesia in 1883 (Verbeek, 1983, 1885; Siswowidjoyo, 1983) and Ritter Island, Papua New Guinea in 1888 (Johnson, 1987; Ward and Day, 2003; Simkin and Fiske, 1983; Day et al., 2015). During the Krakatau eruption, there were 19 tsunamis, with the most destructive generated during the final, cataclysmic, caldera collapse and the associated emplacement of pyroclastic flow material into the sea, which destroyed the volcanic edifice and caused 33,000 fatalities. The Ritter Island tsunami was generated by a ~5 km^3 flank collapse, which is the largest recorded volume lost from an island volcano in a single event historical times (Ward and Day, 2003; Watt et al., 2019). Johnson (1987) estimated that 3,000 fatalities resulted from this event, but other (largely upublished) evidence and anthropology studies (Dunbar, 1993), indicate a total number of death of 700 to 1,000 is more likely. Because of the paucity of data on most volcanic events, the results of their tsunami modelling have not been fully validated and both landslide source mechanisms (e.g., Hunt et al., 2011; Ward and Day, 2003; Watt et al., 2019) and the generated tsunamis (e.g., Day et al., 2005; Løvholt et al., 2008; Abadie et al., 2012, 2020; Tehranirad et al., 2015), remain poorly documented, so are a challenge to model. With remarkable prescience, Giachetti et al. (2012) modeled a tsunami from a collapse of the SW flank of the Anak Krakatau (AK) volcano, similar to that of Dec. 28th 2018, using a hypothetical 0.28 km^3 volume. The resulting wave heights and arrival times along surrounding coastlines foreshadowed the 2018 event.

In the evening of December 22, 2018, at 20:55-57 local time, following a 6 month period of relatively heightened eruptive activity, a lateral collapse occurred on the southwest flank of the AK volcano in the Sunda Strait, Indonesia (Figs. 1 and S1). The collapse generated a tsunami that flooded the adjacent coastlines of Java and Sumatra within 30 minutes (Grilli et al., 2019), causing up to 13.5 m runups and resulting in 437 fatalities, 13,000 people injured, 33,000 displaced and thousands of buildings destroyed (AHA, 2018; Andersen, 2018; Muhari, 2018, 2019; Grilli et al., 2019; TDMRC, 2019). The AK event was the most damaging volcanically-generated tsunami since the 1883 eruption of Krakatau and the 1888 lateral-collapse of Ritter Island. The numerous observations made of AK's 2018 collapse and tsunami, including those previously unpublished by the authors of this paper, provide a unique dataset for both understanding this event and testing state-of-the-art tsunami modelling methodologies against direct observations, with the modelling constrained by both volcanic tsunami source parameters and observations of the generated waves and their coastal impact.

Here we report on and compare the validity of hypothetical volcanic lateral-collapse scenarios with data from an actual event at AK. Our modelling is based on a comprehensive subaerial and submarine data set, including from our 2019 marine survey, of the 2018 AK lateral collapse (Hunt et al., 2020). The subaerial data on the collapse has been published (e.g., Williams et al., 2019; Novellino et al., 2020; Perttu et al., 2020) and provided the basis for previous tsunami modelling (e.g., Grilli et al., 2019). The new numerical modeling presented hereafter is also based on this remote (mainly satellite) subaerial data but also, for the first time, on a hydroacoustic data set of multibeam echosounder (MBES) bathymetry and seismic data acquired to the southwest of the volcano after AK's eruption, in August 2019 (Priyanto et al., 2020; Hunt et al., 2020).

An important aspect of our new modelling of the 2018 collapse and tsunami generation is to use the latest version of the three-dimensional non-hydrostatic model NHWAVE (Zhang et al., 2021a,b), that features effects of vertical accelerations, not just in the water (as in earlier implementations) but also within the slide material itself. Previous published modelling has neglected vertical acceleration (i.e., non-hydrostatic) effects within the slide layer. We show that including these effects is important for an accurate simulation of both wave generation from the collapse and the near-field runups. These new simulations are also performed at a much higher resolution, owing in part to the new high-resolution bathymetric and topographic data from our 2019 field survey and its subsequent analyses and reconciliations with the subaerial observations (Hunt et al., 2020). Model results for both the near- and far-field tsunami generation, propagation and coastal impact are validated against time series of sea surface elevation recorded at tide-gauges in the Sunda Straits together with all published field observations and eyewitness accounts to date of onland tsunami flow depth and runup, both on islands in close proximity to AK (including the August 2019 authors' drone survey), and in the far-field on the coasts of Java and Sumatra.

The combined subaerial and marine data sets, and results presented here, constrain the style of the AK lateral collapse and also test current volcanic landslide-tsunami models, which can be used to predict the behavior of similar events at other volcanic islands. The results, therefore, are an important contribution towards improved assessment of tsunami hazard from analogous events in the future, and also provide an improved basis for developing mitigation strategies for volcanic tsunamis.

2 Background and earlier modeling work

2.1. Geologic and volcanologic context

AK (Fig. 1) is a composite volcanic cone that developed on the northeast margin of the 250 m deep flooded caldera formed by the 1883 eruption of Krakatau (Fig. 2d; Camus et al., 1987; Stehn, 1929). It developed from and so is aligned with the feeder vents of the 1883 Krakatau eruption (Verbeek, 1885, 1983). During the past 90 years of frequent eruptive activity, AK has grown from a submarine volcano to a subaerial edifice, emerging in 1929. With a pre-2018 collapse height estimated at about 335 m (Grilli et al., 2019), it formed an island with a diameter of 1.5-2 km. On the SW flank of AK, coastline retreats of several hundred meters in 1934, 1935 and 1950 (Stehn, 1929) imply long-lived instability of the edifice on this sector. The NW-SE orientation of the retreats align with both the underlying caldera-wall scarp and the 2018 collapse scar (Fig. 2d). The retreats are a result of: i) AK's location on the margin of the 1883 caldera; ii) the volcano is on the northeast margin of the 250 m deep intra-caldera basin; and iii) the asymmetrical pattern of island

Commented [AMN2]: This might be silly of me, but I'm unsure how this differs from the previous point?

growth (see discussion in Hunt et al., 2020). The early submarine activity of AK before and during first emergence of the island in 1929 was dominated by phreatomagmatic explosions (Umbgrove 1928; Stehn 1929). Similar explosions continued after first emergence and built-up a low-angle tuff cone around a vent to which the sea continued to gain access until the 1960s. At that time the vent dried out and further subaerial eruptive activity produced lava flows on the SW side of the island, and Vulcanian and Strombolian scoria (Siswowidjoyo, 1983). This activity continued into the 21st Century, with numerous small eruptions punctuated by more violent explosive episodes, and built-up of a steep-sided central pyroclastic cone, with lava deltas extending the island on most sides except the sheltered NE where the tuff cone was widest, but especially in the NW and SE (Abdurrachman et al., 2018). During a subaerial eruption in 1981 (Camus et al., 1987), a ~2 m high tsunami was recorded on Rakata, a remnant of the 1883 volcanic island and the southernmost and largest island of the contemporary Krakatau archipelago (Fig. 1), which was inferred to originate from a small flank landslide. The event highlighted the potential instability of the southwest flank of the volcano (Camus et al., 1987) but, apart from this, no other tsunamis from AK have been reported.

Commented [SG3]: From Simon

The recent period of AK volcanic activity started in June 2018 and continued into December (https://volcano.si.edu/volcano.cfm?vn=262000), producing Strombolian explosions, lava flows, and ash plumes reaching altitudes of up to 5 km (Anon, 2018; Fig. 2 in Paris et al., 2020a; Figs. S1c,d;). On Dec. 22, 2018, a major lateral collapse occurred on AK's southwest flank which discharged volcaniclastic material into the sea and triggered a destructive tsunami (Andersen, 2018; PVMBG, 2018). Based on seismic records (Gurney, 2018), eyewitness reports (e.g., Andersen, 2018; Perttu et al., 2020), and the agreement of modelled waves with tsunami arrival times at tide gauges (Ina-COAP, 2019; see below; Fig. 1a, Table 2), Grilli et al. (2019)

estimated that the collapse took place at 20:55′–57′ (UTC + 7), a time range later confirmed and used by other authors of numerical models (e.g., Borrero et al., 2020; Mulia et al., 2020; Paris et al., 2020a; Zengaffinen et al., 2010), and confirmed in the interpretation of seismic signals by Walter et al. (2019), who timed the collapse at 20:55′. Within 30 minutes of the collapse a tsunami flooded the coasts of west Java and southeast Sumatra, causing up to 13.5 m on land runups. The tsunami struck near high tide (+1.5 m over MSL in average at four tide gauge in Java and Sumatra; Fig. 1a), which increased its impact (AHA, 2018; Muhari, 2018, 2019; Grilli et al., 2019; TDMRC, 2019).

2.2. Previous modeling of the 2018 AK event

In light of the modelling published by Giachetti et al. (2012), Grilli et al. (2019) performed the first comprehensive numerical simulations of the Dec. 22nd 2018 AK collapse, based on satellite observations on the days following the event, drone and field surveys of near-field tsunami impact conducted in early January 2019 (Reynolds, 2019; TDMRC, 2019; Fig. S1), and historical data on the growth of AK (e.g., as in Fig. 2d). The modelling of AK's flank collapse and tsunami generation was based on a range of failure surfaces with corresponding collapse volumes of 0.22-0.30 km^3 and used the three-dimensional (3D) non-hydrostatic (NH) model NHWAVE (Ma et al., 2012, 2015; Kirby et al., 2016), in which the collapse was represented by a depth-integrated (hydrostatic) layer of a granular material or dense viscous fluid. From the modelling it was proposed that a 0.27 km^3 collapse volume caused the tsunami that best reproduced the near- and far-field tsunami propagation and impact, with the far-field modeling using the fully nonlinear and dispersive Boussinesq model FUNWAVE (Shi et al., 2012).

Numerical simulations of the 2018 AK collapse and tsunami post-dating Grilli et al. (2019), detailed in the following, were also based on hypothetical source parameters derived from a variety of, mainly indirect, data. In these studies, the various assumed/hypothetical failure surfaces gave collapse volumes in the range ≈ 0.14-0.33 km^3, which were both smaller and larger than the 0.27 km^3 of Grilli et al.'s (2019). In Ye et al.'s (2020) study, inversion of broadband seismic data was used to infer a collapse volume of ≈ 0.20 km^3. In some studies, an empirical analytical or experimental (from laboratory tests) landslide source was specified directly on the free surface without an actual modeling of the source (e.g., Heidarzadeh et al., 2020; Borrero et al., 2020). In other modeling studies, new interpretations of subaerial observations were used (see Hunt et al., 2020 for a discussion) and the flank collapse and tsunami generation modeled for a variety of volumes and geometries, in a way similar to that of Grilli et al. (2019) (e.g., Mulia et al., 2020; Ren et al., 2020; Omira and Ramalho, 2020; Paris et al., 2020a; Zengaffinen et al., 2020; Dogan et al., 2021). In the latter models, tsunami generation was based on various rheologies (granular, viscoplastic, Bingham) and simulated using a two-dimensional (2D) two-layer model. There were also important differences in tsunami propagation models used in these various studies, with some using a dispersive model as in Grilli et al. (2019) (e.g., Mulia et al., 2020; Paris et al., 2020a; Borrero et al., 2020) and others using a non-dispersive tsunami propagation model (e.g., Heidarzadeh et al., 2020; Ren et al., 2020; Omira and Ramalho, 2020; Dogan et al., 2021). As landslide tsunamis are typically made of shorter, more dispersive, wave trains, they often require the use of a dispersive long wave model for their accurate modeling (e.g., Ma et al., 2012; Glimsdal et al., 2013; Tappin et al., 2014; Grilli et al. 2015, 2017; Schambach et al., 2019). For the 2018 AK event, Paris et al. (2020a) concluded that dispersive effects were important during tsunami generation and propagation, whereas Zengaffinen et al. (2020) found that they were not large in the shallow water areas of the Sunda Straits (as could have been expected), to the north and south of AK. More specifically:

- In one of the more comprehensive recent studies, Zengaffinen et al. (2020) modeled the tsunami using the rate of mass release, the landslide volume, the material yield strength, and orientation of the landslide failure plane, together with the 2D two-layer depth-averaged coupled model BingClaw, to identify different failure mechanisms, landslide evolution, and tsunami generation. The depth-integrated landslide layer was based on a viscoplastic flow rheology, coupled with depth-averaged long wave and shallow water type models to simulate tsunami propagation. With a volume of 0.28 km^3, identical to that of Giachetti et al. (2012), the numerical simulations provided a reasonable match to the observed tsunami surface elevation amplitudes and inundation heights in the far-field. Overall the results were consistent with those of Grilli et al.'s (2019) preferred 0.27 km^3 scenario, and discrepancies between the simulated and observed arrival times at the offshore gauges were attributed to the (poor) accuracy of the available bathymetry, rather than to their model. To match these, to the north of Krakatau, Zengaffinen et al. (2020) arbitrarily increased the water depths in this area.
- Paris et al. (2020a) used the 2D two-layer depth-averaged coupled model AVALANCHE, which features a granular rheology and a Coulomb friction for the slide description, with dispersive effects for the water flow part. From pre- and post-collapse satellite and aerial images, and a satisfactory comparison of the simulated water waves with far-field observations (tide gauges and field surveys), they reconstructed a total (subaerial and submarine) landslide volume of 0.15 km^3, at the lower end of the volume range in the various studies described here.
- Ren et al. (2020) applied a 2D two-layer depth-averaged coupled non-dispersive model throughout, with the slide layer modeled as a dense fluid. Using two nested grids, the smaller

having a 30 m resolution and the larger a coarse 230 m resolution, and 0.2-0.3 km^3 collapse scenarios, they showed a reasonable agreement with the first wave at the far-field tide gauges.

- Mulia et al. (2020) integrated the landslide thickness over the estimated source area and, assuming a failure surface similar to that of Giachetti et al. (2012), except for a slightly steeper slope, obtained a collapse volume of 0.24 km^3 (slightly smaller than that of Giachetti et al., 2012, and Grilli et al., 2019). Using the 2D two-layer depth-averaged coupled model VolcFlow simulating avalanche dynamics (here assuming a constant retarding stress throughout), and FUNWAVE for the far-field tsunami, their landslide generated higher than 40 m waves in the vicinity of the volcano. As with other studies the tsunami attenuated rapidly as it propagated away from the generation area, resulting in lower than 2 m wave heights at tide gauges around the Sunda Strait.
- Finally, in the latest study to date, Dogan et al. (2021) modeled a 0.25 km^3 collapse (based on a maximum elevation for AK of only 260 m, smaller than used in other studies), and its tsunami generation, using Imamura and Imteaz (1995)'s two-layer long wave model. Tsunami propagation to the far-field was then simulated using the non-dispersive NSW model NAMI DANCE, in an 80 m resolution grid. Little details are given of the parameterization of their dense fluid rheology in the slide model or the rationale for defining the pre- and post-failure volcano geometry, including the selected failure surface. However, they show a good agreement with both arrival times and elevation time series measured at the 4 tide gages in Java and Sumatra. Based on observed bathymetry changes in pre- and post-event surveys, they model tsunami generation from additional submarine slope failures on the north and south sides of the caldera, but conclude that these did not contribute to and hence were not simultaneous with AK's 2018 event.

ADD TABLE SUMMARIZING EARLIER MODELING STUDIES AND THEIR FEATURES ?

All of these studies used different AK collapse scenarios and a wide spectrum of approaches and tsunami modelling, but the differences in tsunami elevations predicted at the far-field tide gages were small; there were larger differences in predicted far-field runups, but some of these could be explained by differences in grid resolution and model physics. While details of a tsunami source become less important when the distance from the source increases, here, the small differences in the predicted far-field tsunami impact between various modeling studies were in great part because the landslide mechanisms were based on inverse methodologies and, hence, were partly or wholly hypothetical. So, although the recorded far-field tsunami was reproduced, it was not based on the actual collapse mechanism but, at best, on direct evidence such as from satellite imagery, or indirect evidence such as from seismic observations of the subaerial collapse. In all studies, submarine data to confirm the submarine components of the landslide source mechanism was lacking. In the modelling studies using a semi-empirical landslide source (e.g., Borrero et al., 2020; Heidarzadeh et al., 2020), the collapse volume and hence source strength were adjusted based on field observations (e.g., near- and/or far-field runup and tide gauges). The validation was then from the forward numerical modeling of the tsunami, which is rather circular. Other modeling studies using an actual slide model also adjusted or confirmed their collapse scenario and volume, among a range of those, based on achieving a good agreement of tsunami simulations with far-field data.

While making some adjustments of the source to best match the far-field observations, most of the previous studies also demonstrated a moderate sensitivity of the predicted far-field tsunami impact to the landslide source characteristics. This shows that far-field tsunami observations alone cannot fully constrain the 2018 AK collapse parameters and, hence, stresses the need for also using near-field tsunami data and, more importantly, marine surveys to do so, as will be done in this work.

3 Methods

3.1 *Study area, computational grids, and bathymetric/topographic data*

Figure 1a shows the entire study area and the footprint of the two computational grids used in the simulations of: (G2) AK's collapse and tsunami generation/near-field impact with the 3D model NHWAVE; and (G1) tsunami propagation and far-field impact with the 2D model FUNWAVE, together with their bathymetric and topographic data.

The near-field Grid G2 is defined with a $\Delta x = \Delta y = 30$ m horizontal resolution (Table 1), from the composite bathymetry developed by Hunt et al. (2020), based on the new multibeam echosounding (MBES) bathymetry acquired during their August 2019 field surveys (Figs. 2a,b), combined with: (i) unpublished Sparker seismic reflection profiles acquired in 2017; (ii) basin bathymetry from Deplus et al. (1995) manually modified within the deep part of the caldera to add up to 10 m of sediment infill between 1995 and 2018 (based on interpreted seismic profiles in Hunt et al., 2020); (iii) an 8 m DEM for the islands of the Krakatau archipelago (from http://tides.big.go.id/DEMNAS); and (iv) topography from Gouhier and Paris (2018) for AK itself, based on the DEMNAS DEM, with modifications to account for island growth in 2018.

Commented [SG4]: Simon suggests discussing uncertainties in processing bathymetric survey data. But this was done I think in the Nature Comm paper

The far-field grid G1 (Fig. 1a; Table 1) is Cartesian with a 50 m resolution and its bathymetric and topographic data is interpolated from Giachetti et al. (2012)'s 100 m resolution dataset. Note that even though the bathymetric data is coarser than the model grid, using a finer model grid than, e.g., the 90 m resolution used by Grilli et al. (2019) allows for a more accurate resolution of the nearshore wave physics.

Regarding the reference mean water level (MWL), when the tsunami was generated, the average elevation at the four tide gauges (WG 6-9; Fig. 1a; Table 2) was approximately +1.5 m over mean sea level (MSL), to which the bathymetry is referenced. Hence, this value was added to the interpolated bathymetric data for both Grid G1 and G2, prior to performing tsunami simulations (i.e., MWL = MSL + 1.5 m). When comparing to field data specified to be referenced to MSL, a 1.5 m correction was subtracted to the field data before comparing it to results of tsunami simulation.

3.2 *Landslide source model*

The landslide source model was defined on the pre-collapse bathymetry/topography grid G2 defined above, using constraints that drew on the post-collapse bathymetric survey of Hunt et al. (2020), particularly to define the boundaries of the submarine failure surface, as well as an updated interpretation of the subaerial failure plane. The latter was based on a sequence of Synthetic-Aperture Radar (SAR) satellite images collected in the days following the collapse, alongside aerial imagery collected on Dec. 23rd 2018. These images proved particularly important in defining the northern and southern bounds of the subaerial collapse scar, since their position could be precisely defined based on the complex coastal shape of the lava deltas. The COSMO-SkyMed SAR imagery from Dec. 23rd 2018 confirms the shape of the failure scar between these two coastal points (cf. Hunt et al., 2020) and was used to pick both the upper line of the headwall and the point where this intersected sea-level (i.e. the 0-m contour; e.g., Figs. 2d,e). These two boundaries were used to define the subaerial dimensions of the modeled landslide failure plane, and we thus consider this component of the failure surface to be fixed in the range of source models described below.

To address the limitations of the published tsunami source models of the collapse mechanism and the landslide resulting from the 2018 AK flank collapse, MBES bathymetry and seismic data were acquired in the 250 m deep basin on the southwest flank of the volcano in August 2019 (Hunt et al.,2020). From detailed analyses of this marine survey data (Fig. 2a-c) these authors mapped the submarine landslide resulting from the volcanic collapse and estimated the landslide outrun deposit volume at, 0.214 ± 0.036 km^3. Rather than being volcanoclastic material, the submarine deposit is mainly composed of large intact blocks (Figs. 2a-c), confirming that the event occurred as a single *en masse* slide with limited fragmentation, rather than in a more piecemeal, staged process. This mechanism is also confirmed by seismic data (Gurney, 2018). From these characteristics, while there were many large landslide blocks in the deposits (up to hundreds of meters across), a granular slide rheology was deemed more relevant in our subsequent modeling than a dense fluid rheology, which is more appropriate for debris flows (although both were simulated for completeness). An additional unit, to the southwest of this main deposit, with a volume of 0.022 ± 0.006 km^3, was interpreted as a secondary sediment failure (i.e., debris flow), triggered by the primary landslide emplacement.

Commented [AMN5]: Perhaps say why?

Based on the marine survey, a range of volumes were identified for the 2018 AK collapse, in combination with new analyses of subaerial observations from high-resolution satellite imagery and aerial photography that estimated the subaerial collapse volume to 0.098 ± 0.019 km^3 (cf. Hunt et al., 2020), and a new interpretation of the historical growth of AK (Fig. 2d). Thus, beneath sea level, the lateral margins of the collapse scar were defined using bathymetric features on the submerged flank of AK evident on the post-collapse marine survey. A subtle step in the submerged SW flank, at about -120 m, that may correspond to the base of the failure plane, was used to define the minimum collapse volume scenario (Fig. 2e), which has a shallower failure surface than that

Commented [SG6]: Later on we use -80 m for the shallowest and -220 m for the deepest. We need to reconcile…

of Grilli et al. (2019) for their minimum 0.22 km^3 volume scenario, yielding a minimum collapse volume of 0. 16 0.175 km^3. Identification of this shallow failure surface was still uncertain, however, because of burial by post-collapse deposits. Additional features on the NW and S flank of AK, that align with the subaerial margins of the scar, alongside deeper features on the SW flank (cf. Hunt et al., 2020), were used to define a larger, deeper-seated failure surface, whose volume was estimated at 0.272 km^3 (Fig. 2e). Both end point collapse volumes include a 0.098 km^3 subaerial component.

Comparing the volumes estimated purely from the MBES survey to those estimated based on the failure surface location and geometry, we find good consistency. The main part of the landslide deposits forms a blocky mass, identified in the August 2019 MBES data (Figs. 2b,c) and interpreted as representing material directly derived from the island flanks, with a volume of 0.214 ± 0.036 km^3. A more distal part of the deposit is interpreted as a secondary debris flow, resulting from sediment mobilized by landslide emplacement and seafloor incision, with a volume estimated to, 0.022 ± 0.006 km^3. The estimated primary deposit volume of 0.214 km^3 lies between the two end-point failure-surface-derived volumes described above (Fig. 2e). Given that the mass is likely to have expanded upon fragmentation, and is potentially bulked via seafloor erosion, this suggests that an increase in the volume of the landslide, compared to the maximum volume derived from the shallower failure surface, can be accounted for by these phenomena. Additionally, some of the failed mass could have remained within the scar region and been subsequently buried; hence, it would not be included in the MBES estimate of deposit volume. Consequently, we cannot reject a scenario with a deeper-seated failure plane and a larger volume of 0.272 km^3 based on the MBES surveys, although our interpretation is that the primary failure volume was likely closer to our minimum estimate (0.175 km^3).

Commented [sw7]: See my comments below – in Hunt et al. the value is 0.16, but we need to check the origin of this with James, as our final landslide surface (minimum) comes up with a volume of 0.175 which corresponds to your lowest modelled volume. It would be better to make the two papers consistent if James is happy to update his volume.

Commented [SG8]: To be reconciled with Hunt et al

Commented [SG9]: To be reconciled with Hunt et al.

Within the blocky landslide deposit (Fig. 2b,c), it can be assumed that transport of all material derived from the volcano flanks was tsunamigenic. Because of the potential for expansion and incorporation of seafloor material, we use the scar-derived volumes to define the range of source-volumes for tsunami modelling. In addition to this, mobilization of seafloor sediment triggered by primary landslide emplacement (forming the secondary debris flow deposit) may also have contributed to tsunami generation. However, given that this must have followed the main stage of landslide motion, was in relatively deeper water, and was an order of magnitude smaller in volume, we assume that this material was not significant in contributing to the main tsunami generation. The debris flow volume also falls well within the range of uncertainties of the estimated landslide volume.

In the modeling, the above uncertainty in AK's collapse parameters is represented by defining four landslide (and failure surface) geometry and corresponding volume scenarios, for which we use the same subaerial pre-collapse geometry in every case (based on the SAR-derived collapse-scar position), intersecting the NE flank at about 100 m elevation (Fig. 2e). For the submarine surface, we use the minimum and maximum bounds of the failure surface described by Hunt et al. (2020) and discussed above, along with two intermediate scenarios, defining maximum depths on the SW flank ranging from -80 to -220 m (Fig. 2e). All four failure surfaces cut the active vent position at depths ranging from 25 to 40 m, which is consistent with the vigorous Surtseyan eruptive activity that immediately followed the collapse. Based on the pre-collapse AK topography (maximum 335 m), refined based on high-resolution satellite images (Novellino et al., 2020) the volumes associated with these 4 scenarios were computed to: (1) 0.313; (2) 0.272; (3) 0.224; and (4) 0.175 km^3. The latter two compare closely with the deposit volume estimate, given uncertainties and allowing for some degree of expansion, while the first two scenarios are larger,

Commented [sw10]: -80 based on my model, but again I'm just a bit concerned this is inconsistent with some of the text described by James, even though it uses the same definition of the failure limits. In his paper he describes the step at -100 to -120m, so I need to discuss with him so that we can ensure the two are as consistent as possible. He doesn't clearly show the maps of the failure surface in the main paper (perhaps in the supplement, but I don't have a copy of the final ones he submitted), but the model is based on the outlines agreed with him, so while I'm happy that they match we need to ensure that the descriptions match as far as possible between the two papers, as there is some inconsistency in the numbers at the moment.

Commented [sw11]: This matches the volumes I calculated, and they should also be the same as those described in Hunt et al.

Commented [SG12]: Simon asks to discuss "degree of expansion". Dilation should be included in the model (I agree it would be good but it is not yet included in NHWAVE). We can add that to the discussion as a source of uncertainty to consider in future improvements.

but consistent with some bathymetric features and the possibility that some of the failure mass remained within the collapse scar. The first scenario is close to the largest volume originally simulated by Grilli et al. (2019), and the second is close to that of their likeliest scenario. Among these scenarios, the third one, with a 0.224 km^3 volume, is the estimated mean landslide deposit volume plus 50% of the debris flow and hence is deemed our preferred (or likeliest) volume scenario in terms of providing the best representation of the tsunamigenic mass movement consistent with the MBES survey. The post-collapse bathymetry for this scenario is shown in Figs. 1c and 3b. Note, the latter figure shows that the specified failure surfaces are not planar but slightly concave. This is a necessary shape given the relatively steep gradient (30-40 degrees) of the subaerial failure plane (constrained from SAR imagery and consistent with the volcanic vent being cut beneath sea-level) but the need for the foot of the failure to emerge within the submerged flank of AK, and is also typical of the morphology of volcanic lateral collapses.

Commented [AMN13]: This could be better worded.

3.3 *Tsunami generation and propagation simulations*

3.3.1 *Numerical tsunami models.*

Two numerical models are used in simulations of AK's 2018 collapse and tsunami generation, propagation and coastal impact, which are briefly described below.

NHWAVE (Ma et al., 2012), a three-dimensional (3D) non-hydrostatic model, is used to simulate both AK's volcanic collapse scenarios, and the corresponding tsunami generation and near-field impact, on AK and surrounding islands, in Grid G2 with a 30 m horizontal Cartesian grid with 1,155 by 9,55 cells, using 7 boundary fitted water layers in a vertical σ-coordinate system (Figs. 1b,c; Table 1). With one layer, the model provides the same order of dispersion as a Boussinesq model such as FUNWAVE, detailed hereafter, and higher-order dispersion effects when using more layers. NHWAVE has been used, and experimentally validated (e.g., Ma et al., 2012), to model tsunami generation from solid slides (landslides or slumps) (e.g., Grilli et al., 2015; Schambach et al., 2019) and from dual sources coseismic/solid submarine mass failures (Tappin et al., 2014). NHWAVE was extended to simulate tsunami generation by deforming slides, both submarine and subaerial, assumed to behave as either a granular medium or a dense Newtonian fluid (Ma et al., 2015; Kirby et al., 2016). These NHWAVE models were applied to case studies for deforming slide sources (e.g., Grilli et al., 2017b, 2019; Schambach et al., 2019), and validated based on laboratory experiments for those studies (Grilli et al., 2017b), as well as for dual sources involving a combination of coseismic and deforming underwater/subaerial slides (e.g., Grilli et al., 2019; Schambach et al., 2020a,b).

Since the work of Grilli et al. (2019), a new version of NHWAVE has been developed (Zhang et al., 2021a,b) that includes effects of vertical acceleration (i.e., non-hydrostatic pressures) within the slide material layer, which was neglected in the earlier implementation (Ma et al., 2015). Considering the steep slopes of both AK and the surrounding islands, it was anticipated that such effects might be important. This was confirmed here by comparing, in Supplementary file #2, simulations of the Grilli et al. (2019) preferred volume scenario (0.272 km^3), with both a granular and viscous rheologies, and with and without the non-hydrostatic effects included in the equations for the slide layers. Results for both rheologies showed that slide motion and wave generation are significantly affected, with larger waves generated and much larger runups occurring on the near-field islands, particularly Panjang and Sertung, when non-hydrostatic effects are neglected. When comparing with near-field runup measured in field surveys, a much better agreement was obtained with the newer version of the model that accounts for non-hydrostatic effects within the slide layer.

For these reasons, this newer version of NHWAVE by Zhang et al. (2021a,b) was used in the present study.

FUNWAVE-TVD (Shi et al., 2012; version 3.0 is used), a two-dimensional (2D) fully nonlinear Boussinesq wave model, is used to simulate far-field tsunami propagation and coastal impact in Cartesian Grid G1 with a 50 m resolution and 3,900 by 3,680 cells (Fig. 1a; Table 1), which is acceptable in view of the small geographic area considered here. To improve dispersive properties, the horizontal velocity used in this Boussinesq model is that at a depth $z = -0.531\, h$. To prevent reflections from the open boundaries of grid G1 (Fig. 1a), 10.8 km (or 216 grid cells) wide sponge layers are specified along its 4 boundaries.

Both NHWAVE and FUNWAVE-TVD used a Courant number and Froude cap condition to adaptively specify the time step in simulations to achieve optimal accuracy. In shallow water and during runup this can lead to using prohibitively small time steps, which is prevented here by specifying a minimum depth truncation of 1 m and 0.05 m in the NHWAVE and FUNWAVE simulations, respectively. The 0.05 m minimum depth has little effect on FUNWAVE simulations of the far-field tsunami impact. In the near-field, considering the very large waves and runups modeled with NHWAVE, the 1 m minimum depth also does not significantly affect simulation results. Both models are parallelized with MPI, allowing to efficiently run them on large computer clusters. Here we typically used 20 processors to run each scenario. Finally, both models are open source and available on *github*, together with their user manual and benchmarking examples.

3.3.2 *Modeling methodology.*

Simulations of AK's collapse and tsunami generation and near-field impact are first performed in grid G2 with NHWAVE, for the 4 volume scenarios, and for each of those, assuming either a granular or a dense fluid rheology. When the slide is fully at rest and waves approach the boundary of grid G1 (Fig. 1a), NHWAVE results for surface elevation and horizontal velocity interpolated at 0.531 times the local depth are used to initialize FUNWAVE simulations in Grid G1. These are then run for another 2h of tsunami propagation time, to make sure all the diffraction, and multiple reflection effects on the tsunami from the shores and many islands of the Sunda Straits are included in the results.

In NHWAVE simulations, for each of the 4 specified collapse surfaces and volumes (Fig. 2e), we use the same parameterization of the slide rheology as in Grilli et al. (2019), i.e.: (i) a Newtonian fluid of density ρ_c = 1,550 kg/m^3 and the kinematic viscosity of a debris flow, ν_c = 0.5 m^2/s; or (ii) a granular medium with ρ_c = 1,900 kg/m^3 for the solid part and similar to Giachetti et al. (2012), an internal friction angle ϕ_{ic} = 10°, a basal friction angle ϕ_{bc} = 2°, and a 40% porosity. With this data, assuming a water density ρ_w = 1,025 kg/m^3, the average density of the granular medium is ρ_{ac} = 1,550 kg/m^3. For each of these 8 scenarios, NHWAVE was run up to 410 s; however, results showed that the time when the generated tsunami waves approach the boundary of grid G1 is t = 380 s (e.g., Fig. 7h), which is used to prevent any perturbation of the solution.

Finally, in both model grids, in the absence of site-specific data we specify a constant bottom friction coefficient C_d = 0.0025, which corresponds to coarse sand. While this value may be too small to model friction on the rough walls of the caldera to the SW of AK, earlier work has shown that bottom friction only significantly affects tsunami propagation (in particular reduces tsunami elevations) over shallow areas where propagation distances are many dominant wavelengths (Tehranirad et al., 2015). In this case, the bottom velocity caused by the long tsunami waves (in terms of wavelength to depth ratio) is consistently large. Considering the fairly short dominant period of the generated waves, here, bottom friction will only significantly affect tsunami propagation towards Java and Sumatra, in the shallow eastern side of the Sunda Straits. In the caldera to the SW of AK, however, both the water depth is large and the tsunami propagation distances are short, and bottom friction effects are thus expected to be small; hence, the accuracy of the selected C_d value is not important.

3.3.3 *Computation of flow depth and runups based on model results*

For all modeled scenarios, the pre- and post-processing of NHWAVE and FUNWAVE input data and results was done using Matlab codes custom-developed for this purpose. Results produced include most of the figures shown in this work, animations of model outputs provided in supplementary material and, where available, a comparison of numerical simulations to field data. In this respect, specific algorithms were developed to accurately extract the maximum tsunami flow depth along the shore (0 m contour in MWL), and runup from model results. In both cases, this was done for: (flow depth) by computing the location of the 0 m bathymetric contour in the bathymetric/topographic data; and (runup) by computing the location of the 0 m elevation contour in the maximum elevation minus bathymetric/topographic data set. Then, the envelope of maximum computed surface elevation (e.g., Figs. 8 and 9d) was interpolated along both contours to yield the flow depth and runup data along the selected coastline (e.g., Figs. 14-16). Note that to clarify the visualization of these results, 4 classes of elevations were selected and color coded as: (yellow) 0-1 m; (green) 1-2 m; (red) 2-4 m, and (pink) > 4 m; dots with this color code were plotted both in plan view along the coast and in elevation figures to be compared with field data (e.g., Figs. 14, 16).

3.4 *Tsunami field survey data*

To validate our numerical model results, we used a comprehensive set of data, including marine field surveys, satellite images, bathymetric data as discussed above, and onshore surveys of tsunami impact (Figs. 12-16). The inshore survey data included: (i) the tree line drone survey conducted on Rakata, Sertung and Panjang during our August 2019 field campaign (Figs. 11, 13), and (ii) the runup and flow depth measurements made in the near- and far-field by TDMRC (2019), Muhari et al. (2019), Putra et al. (2020), Borrero et al. (2020), and Heidarzadeh et al. (2020). In addition, we used the extensive video made by Reynolds (2019), during his 01/11/2019 near-field drone survey of AK and the three surrounding islands, of which salient images were extracted by Grilli et al. (2019) (see their supplementary Fig. S8). One example is in Fig. S1f. These surveys show that, in the near-field, the tsunami generated by AK's 2018 collapse caused up to 85 m runups on the islands of Rakata and Sertung and, in the far-field, up to 13.5 m runups on the nearby coasts of Java and Sumatra.

Additionally, as in Grilli et al. (2019) and all other modeling studies, time series of surface elevations simulated for each scenario are compared with detided free surface elevations measured at 4 tide gauges located at (Fig. 1a; Table 2): (5) Serang, Marina Jambu, (6) Ciwandan, (8) Kota-Angung, and (9) Panjang. Grilli et al.'s (2019) Supplementary file #3 explains how the raw data, measured at a 1 min interval, was detided to obtain the tsunami signal (their Fig. S5) and shows where each tide gauge was located (their Fig. S4), pointing out that each gauge is surrounded by some reflective (or dissipative) coastal structures, not represented in the model grids, that can affect tsunami signal in various ways (including seiching). Table 2 provides the location of each tide gauge, its depth in grid G1 and the arrival time of both a 1 cm tsunami elevation and the first significant wave crest. Fig. 10 shows the complete (detided) tsunami time series measured at each gauge by two different independent instruments operating at each gauge (see details in Grilli et al., 2019); there are some differences (sometimes large) between the measurements of the two instruments at each gauge, which allows quantifying experimental errors. The individual data points in the time series illustrate the coarse 1 min temporal resolution of the measured signal.

4 Tsunami simulation results

4.1 *Slide motion and deposits*

Results of combined NHWAVE-FUNWAVE simulations in Grids G2 and G1 of the 4 volume scenarios ((1) 0.313; (2) 0.272; (3) 0.224; and (4) 0.175 km^3), each with either a granular or viscous rheology, are discussed hereafter.

Figures 4 and 5 show examples of slide motion and free surface elevations simulated with NHWAVE. Fig. 4 first compares results in a vertical plane along a SW transect into AK, for the preferred volume scenario (0.224 km^3), using either a granular or viscous rheology. We see that the change in rheology only moderately affects slide deformation for small times (t < 80 s), and hence corresponding wave generation, but that differences in slide runout are much larger later in time (t ≥ 120 s), although this stage of motion is no longer tsunamigenic as the slide deposits are too deep. At t = 200 s (Fig. 4h) the granular slide deposits have nearly stopped and have mostly accumulated in the caldera, at the toe of AK's failure surface, whereas the viscous slide deposits have moved further onto the caldera bottom and are still moving. While the granular slide deposits appear to be located in the general area where the actual deposits were mapped during the August 2019 marine survey (Figs. 2b,c) (Hunt et al., 2020), the viscous slide deposits have moved beyond this area; hence simulations based on the granular rheology appear to be more consistent with field data than those with the viscous rheology. This is confirmed in Fig. 5, which shows greater details of the 3D granular slide motion and deposits for the same volume scenario. Here in the last panel at t = 420 s (Fig. 5h), we see more clearly where the main slide deposits are located (i.e., their runout) and how thick they are (up to 94 m) at the end of the motion, which appears to be consistent with field observations (Fig. 2c). It should be noted that while the main collapse deposits are to the SW, there is a layer of a few meters of granular material deposited on the opposite, NE side of AK and to the NW and SE, which help cause small additional wave generation in those directions. Given the low degrees of fragmentation evident from the very large blocks in the observed deposit (Fig. 2), these features in model results may not be representative of an actual deposit distribution and are more likely an artifact of a landslide model based on a continuous granular rheology. A similar discrepancy between observed and modeled deposits was noted by Ward and Day (2006) in their study of the 1980 Mount St Helens event, which caused a large debris avalanche.

Videos of computed slide motions with and without surface elevation, and for a granular material or a viscous slide are given in supplementary material for the preferred volume scenario (0.224 km^3); see, AK_slide3D_gran.mp4, AK_ slide3D_visc.mp4, AK_wave_slide3D_gran.mp4, AK_wave_slide3D_visc.mp4.

4.2 *Near-field tsunami generation*

Figures 4 and 7 show snapshots of free surface elevation at times t = 10, 20, 40, 80, 120, 160, 200, and 380 s, computed for the preferred volume scenario and a granular or viscous rheology, and Fig. 6 compares time series of surface elevation computed at the 5 numerical wave gauges (Fig. 1b; Table 2) specified in grid G2, for the 8 modeled scenarios (4 volumes and 2 rheologies). Other snapshots of surface elevations for scenarios not shown here look qualitatively similar to those in Fig. 7. Videos of computed surface elevations are given in supplementary material.

Results in Figs. 4 and 7 show that, in the first 20 s of AK's collapse, a large-scale subaerial slide motion occurs down the volcano, triggering a 50+ m horseshoe-shaped leading elevation wave. From 20-80 s, as the slide moves mostly underwater (for all 4 volume scenarios), an up to

30+ m trough (negative elevation wave) forms near the volcano on the SW side, while the leading elevation wave radiates as a cylindrical crest of decreasing height. Figure 6a shows that these processes are well captured at WG 1, which is located directly SW of AK (Fig. 1b; Table 2); at this site, depending on the scenario, a 25-33 m leading elevation wave arrives at $t \approx 60$ s, followed by a 0-10 m trough. At WG 2 and 3, further NW and SW of the volcano, Figs. 6b,c show that, later in time ($t \approx 175$ s), the large elevation wave and its trough (first depression wave) have essentially propagated radially, with only a small decrease in the crest height. The propagation of the horseshoe-shaped leading elevation and first depression waves, with their gradual directional spreading and reduction in elevation, are clearly seen in Figs. 7c to 7h. As these waves propagate away from AK, however, for $t > 80$ s (Fig. 7d), they start interacting with and running up both the N shore of Rakata and S shore of Sertung, causing very large runups.

To the NE of AK, for $t > 100$ s, we see a significant tsunami impact occurring on Panjang's southern tip (25+ m runup) and, for $t > 150$ s, a more moderate impact on its northern tip, that are due to both the propagation and refraction around AK's bathymetry of the leading horseshoe-shaped wave (Figs. 7d-f) and later on its reflection off Rakata and Sertung. Finally, in Figs. 7g,h, we see that large waves are propagating in the SW, E and N directions away from AK. For the latter two directions, these waves are well captured at WG 4 and 5 (Figs. 6d,e), where we see leading elevation waves of about 4 and 5 m, respectively. Fig. 7h also confirms that at 380 s, the leading waves have not yet reached and interacted with the outer boundary of Grid G2.

Considering the 8 different scenarios, results at WG 1 to 5 in Fig. 6 show that while, overall, all generated waves exhibit the same large-scale characteristics, both a change in collapse volume and rheology affect wave elevation and phase to various extents. Between rheologies, the granular rheology generates slightly smaller leading waves in all cases than the viscous rheology (particularly to the SW), and the larger the collapse volume the larger the wave elevations. [Note that the first conclusion is opposite to that of Grilli et al. (2019) who found that larger waves were generated by a granular slide; this could result from the use here of a much higher grid resolution and the new non-hydrostatic slide model.] At all wave gauges (WG 1-5), the larger leading wave is followed by smaller waves of period as low as T = 30-50 s. Over the 250 m deep caldera, these waves are fully or significantly dispersive. Waves in this period range would be dispersive for depth $h < gT^2/400$ = 3.5-9.8 m, hence for most of their propagation to shore, which justifies using a dispersive long wave model such as FUNWAVE to model AK's collapse far-field tsunami propagation.

Fig. 8 shows the envelope of maximum surface elevation computed with NHWAVE in Grid G2 for the preferred volume scenario (0.224 km^3) and a granular rheology; envelopes for the other scenarios look qualitatively similar and are not shown for the sake of brevity. The figure confirms the large wave generation SW of AK, and shows that large 50-100+ m runups occur on the exposed shores of Rakata and Sertung, and 25 m runup on the south shores of Panjang. These results will be detailed later and compared to field measurements.

4.3 *Far-field wave propagation and coastal impact on Java and Sumatra*

For each of the 8 scenarios, FUNWAVE simulations were initialized with results of NHWAVE in Grid G2 at 380 s (Fig. 7h), interpolated onto Grid G1, and tsunami propagation and coastal impact were simulated up to t = 7,580 s from the start of the event. Figures 9a-c show snapshots of surface elevation computed with FUNWAVE for the preferred volume scenario (0.224 km^3) and granular rheology at t = 380, 1800 and 3600 s. Results for the other scenarios are qualitatively similar. After 30 min, Fig. 9b shows that leading tsunami waves have started impacting the SW coast of Java, around the Kolijaah and Panaitan Island areas (Fig. 1a), are impacting the south facing coast of Sebesi (Fig. 1a), and are about to impact the coastlines at Ujung Kulon and Serang, Marina Jambu (tide gauge (WG) 5; Fig. 1a and Table 2). To the north of the grid, leading waves are also impacting the SE tip of Sumatra; waves are also propagating in the direction of tide gauges (WG) 6-9 (Fig. 1a; Table 2). After 1h of tsunami propagation, Fig. 9c shows a complex pattern of waves in the Sunda Straits, as a result of diffraction-refraction around islands and reflection off the coasts, which justifies performing simulations for a long enough time to capture maximum runup at all locations within Grid G1.

Fig. 9d shows the envelope of maximum surface elevation computed with FUNWAVE in Grid G1, after 7,580 s of simulations, for the preferred (granular) scenario. AK's collapse generated initial waves with a strong SW directionality and a secondary E and N directionality (Fig. 7h), which translates upon far-field propagation into a maximum impact on the SW coast Java and a relatively smaller impact eastward and northward on the coasts of Java and southern Sumatra (see also Fig. 9b). Additionally, wave propagation is affected by a significant bathymetric feature, the moderately steep S-N oriented (around Lon. E. 105.3) linear scarp that divides the shallow eastern half of Sunda Straits from the much deeper Semangka trough to the west (Fig. 1a). As can be seen in Fig. 9b (and in the animation of model results provided in supplementary material), this bathymetric feature causes a wave guiding effect that reinforces waves to the south onto Panaitan Island, where some of the largest flow depths and runups were measured, and also guides some waves to propagate northward. Comparing bathymetric contours with the maximum envelope in Fig. 9d, we see that little tsunami energy propagated west of Lon. E. 105.3, and that bathymetric focusing also occurs towards Ujung Kulon (Fig. 1a), which is another area where very large runups were measured (see later for details of runups).

Surface elevation time series were simulated for the 8 scenarios, combining the four volumes and two rheologies, at the locations of the 4 tide gauges (6-9 in Fig. 1a; Table 2), which are compared to the measured detided surface elevations in Fig. 10. Unlike in the near-field, only small differences (including on arrival time) can be seen here between surface elevations simulated for the 8 different scenarios, indicating that the predictions of the tsunami far-field and impact are less sensitive to details of the collapse scenario assumed for AK (i.e., changes in volume size/geometry and rheology). This was already pointed out by other authors in their discussion of model results (e.g., Heidarzadeh et al., 2020; Borrero et al., 2020), and also explains why studies that assumed an approximate empirical source for AK's collapse or only a 2D two-layer slide model, with source parameters adjusted to match far-field data at the tide gauges and/or elsewhere, performed reasonably well for predicting coastal impact. However, for future hypothetical collapses, in the total absence of field data to calibrate these models, they might not have fared as well in predicting tsunami impact, from a single forward model simulation.

Comparing numerical simulations to tide gauge data, Fig. 10 shows, overall, a good agreement for any scenario, particularly earlier in the time series and more so for WG 6-8 (Figs. 10a-c). As summarized in Table 2, arrival times of the leading crest at each gauge are predicted to within 15–78 s of observations. Considering the 1 min data sampling interval of the gauges, this is an acceptable discrepancy. Later in each tide gauge time series, the phase difference between simulations and observations increases, but the trough-to-crest height of the largest waves are well predicted in the simulations. As indicated before, later in time, the signal at the tide gauges was increasingly affected by any local effects and seiching not resolved and simulated in Grid G1, both due to the limited 50 m resolution and the moderately coarse 100 m resolution of the available nearshore bathymetry and topography. Finally, as reported by eyewitnesses, simulations predict that multiple large waves of fairly short period (2–10 min) impacted the coast, with the second or later waves being the largest.

For each of the 8 scenarios, arrival time at the tide gauges is, to the first-order, governed by wave celerity, which strongly depends on bathymetry and to some extent on frequency for dispersive waves. An additional effect of amplitude dispersion may speed-up wave propagation for the largest waves in the near-field, but this effect will also be similar for all scenarios, as their near-field waves are quite similar (see Fig. 6). This explains the small range in arrival time difference, with the field data listed in Table 2 for the 8 scenarios.

4.4 *Near-field runups*

Grilli et al. (2019) pointed out the intense and continuous phreatomagmatic explosive activity that immediately followed the collapse of AK, both obscuring the skies and discharging large volumes of material that rapidly modified the post-collapse topography of AK and surrounding bathymetry. Hunt et al. (2020) made a detailed analysis of these early stages of AK's post-collapse regrowth, using both satellite images and submarine surveys, and quantified the large changes that took place in AK's coastline and subaerial geometry (e.g., such as Fig. S1b and S1e for AK; see also Novellino et al., 2020). This post-collapse eruptive activity paused on Jan. 11th 2019, and Reynolds (2019) was able to conduct a drone survey of AK and the islands of Rakata, Sertung and Panjang (e.g., Fig. S1f and supplementary 4 in Grilli et al., 2019), that confirmed AK's coastline changes inferred from SAR images. Arguably more important was their documentation of the large runups the tsunami caused on the island of Rakata, Sertung and Panjang. Based on these images, Grilli et al. (2019) estimated that 50+ m runups occurred on Rakata's N shore and Sertung's S shore. Subsequent field surveys in 02/2019 by Borrero et al. (2020) and August 2019 by the authors confirmed and quantified these early observations of near-field tsunami impact, and provided geo-localized runup values reaching 85+ m on both islands (Fig. 11), with additional data on Panjang. However, because Panjang was positioned downwind of AK, extensive ashfall-driven vegetation damage, combined with the steep cliffs on the W coast made the runup line on Panjang difficult to unambiguously identify. Finally, Borrero et al. (2020) also measured runup on Sebesi island, north of Panjang, which we also consider to be part of the near-field tsunami impact (Fig. 1a).

For the preferred collapse volume scenario, with granular material, Figures 12a-c show zoom-ins of the maximum envelope of surface elevation computed with NHWAVE (Fig. 8) onto the NW shore of Rakata, SW shore of Sertung and S shore of Panjang, and Fig. 12d shows a zoom-in on Sebesi of the maximum envelope of surface elevation computed with FUNWAVE for the same scenario (Fig. 9d). The location of our August 2019 drone tree line survey is marked on Figs. 12a,b, and the location of four runups/flow depth measurements made on Sebesi by Borrero et al. (2019) are marked on Fig. 12d (7.5, 9, 2.8, 2.5 m from W to E, respectively); the latter values are consistent with those we estimated during our August 2019 survey of Sebesi, in part based on interviewing eyewitnesses. On both Rakata and Sertung (Figs. 12a,b), our predicted runup line touches or goes over the 50 m contour and parallels the drone survey quite well, except at its highest points; those however occur on steep, nearly vertical, cliff faces (Figs. 11a,c) that are not well resolved with a 30 m horizontal grid. On Panjang, in Fig. 12c, our results show runups of 25-30 m on the island's SW tip, tapering to 8-10 m on the NW part of the western shore; the latter values match those reported by Borrero et al. (2020), who could not make a precise survey due to the difficulty in accessing the island, which is faced by steep cliffs on much of its western side (Fig. 11e). In Fig. 12d, our model results show a close agreement with the 4 measured runups on Sebesi's S and SE shore.

Figure 13 details the near-field runups computed on the 3 islands for the 8 modeled scenarios (4 volumes and 2 rheologies), compared to available runup measurements and our drone surveys. Overall, on Rakata and Sertung (Figs 13a,b), although all scenarios fare quite well, our preferred volume scenario with a granular rheology appears to best match the quantitative field data, as well as images from the 01/11/2019 and Borrerro's et al.'s (2020) 02/2019 field survey (Figs. 11b,d) of these islands. On Panjang (Fig. 13c), all our model results are below our tree line drone survey (Fig. 11e) but, again, this was done along a nearly vertical cliff face, a location where it was difficult to estimate the runup line precisely and which is not well-discretized in our model grid; hence, there is large uncertainty on both these runup measurements and their model simulation. We note that all scenarios predict an 8 m runup on the NW side of the island as was reported by Borrero et al. (2020).

4.5 *Far-field runups*

Far-field flow depth and runups were measured along the coasts most exposed to the tsunami in Java and Sumatra in several field surveys. The first one (TDMRC, 2019 took place in 01/2019, soon after the event) was the only such data available to Grilli et al. (2019) to validate their modeling. However, field surveys were also later performed by Muhari et al. (2019), Putra et al. (2020), Borrero et al. (2020), and Heidarzadeh et al. (2020). Figures 14 to 16 compare model results obtained for our preferred collapse scenario (granular rheology) with this data which, to our knowledge, is all such data available to date.

Figure 14 shows a zoom-in along the coast of Java (Fig. 1a) on the envelope of maximum surface elevation computed with FUNWAVE (Fig. 9d). As detailed in the methods section, both the maximum flow depth at the shore and the runup were extracted from these results and, for clarity, color coded in 4 classes of surface elevation. Due to the complex geometry of the coast, the same values of flow depth and runup were then plotted as a function of longitude and latitude in 4 subfigures (Figs. 14a,b,d,e); on the plan view (Fig. 14c), the color coded flow depth values were plotted along the shore. Fig. 14c shows that, as expected from the tsunami directionality, wave guiding effects offshore, and wave refraction nearshore, leading to focusing/defocusing effects, the alongshore variation of maximum tsunami impact is a highly irregular on SW Java; this causes similarly large alongshore variations in flow depth and runup seen in Figs. 14a,b,d,e. The field data for both flow depth and runup is plotted on top of the elevation figures showing model results, in Figs. 14b,d and. 14a,e, respectively. Overall, there is a good agreement of model results with the field measurements, and more so for flow depth at the coast, which is less sensitive to irregularities of the terrain and the built-up elevation maps, that are not represented in our 50 m resolution grid.

Figure 15 shows zoom-ins of results presented in Fig. 14 in three of the most impacted areas along the coast of Java where field surveys were conducted, namely (Fig. 1a): (PI) Panaitan Island; (UK) Ujung Kulon; and (K) Kolijaah. Model results for the preferred volume scenario (granular rheology) are compared to the locations/values of measured maximum runups, wherever available (Fig. 15e), or otherwise to field data measured by Borrero et al. (2020) marked onto Google Earth images of each site (Figs. 15b,d). These measurements were provided as raw or detided, so here we are plotting their raw values compared to our results with respects to MWL. [Note, Borrero et al. only assumed a 2 cm tide throughout without justification, which will introduce some uncertainty in the comparison; also, their measurements from UK (Fig. 15d) are reported on Figs 14a,e as runup, since these values were measured inland.] At PI (Figs. 15a,b), the model accurately predicts the 6-8.4 m range (referred to MWL) of maximum tsunami elevations measured at the marked locations along an approximate N to S survey from the tip of the island (Fig. 15b,; Borrero et al, 2020). At UK (Figs 15c,d) the model predicts slightly less (6.5 to 9 m) than the 6.9-11.5 m range (referred to MWL) of maximum tsunami heights measured at the marked locations from N to S from the tip of the Peninsula (Fig. 15d; Borrero et al, 2020); however, the largest flow depth was measured at an isolated tree (their Fig. 12) and our 50 m resolution model grid cannot represent this level of detail. Finally, at K (Figs. 15e,f) the model predicts most of the runups (both location and value) measured by Muhari et al. (2019), Putra et al. (2020), and Heidarzadeh et al. (2020), reasonably well. Some of the reported measurement locations show a mismatch, but the majority of measured runups in the 3 surveys align well with our predicted inundation limit. At the K location, the Google Earth image (Fig. 15f) is only provided for reference.

Figure 16 shows results similar to those of Figure 14, for flow depth at the coast predicted along the SW shore of Sumatra for our preferred collapse volume scenario (granular rheology), compared to the available data from field surveys; the agreement between both is quite good here as well. The largest tsunami impact occurred in the area of Waymuli (W in Fig. 1a, around 105.6348 E), of which Fig. 16c shows a picture of the damage taken by Fritz et al. (2019) during their 02/2019 survey.

5 Discussion and conclusions.

New numerical simulations of AK's 2018 collapse and tsunami generation, propagation, and coastal impact were performed with state-of the-art numerical models, including a novel landslide tsunami model for granular and viscous slides that includes non-hydrostatic effects of vertical acceleration in the slide material. Results show that incorporating non-hydrostatic effects is important for accurately simulating tsunami generation and near-field impacts from the AK flank collapse. This is illustrated in the 8 scenarios we used, which combined 2 different rheologies (granular and viscous fluid material) and 4 different volumes obtained from a new parametrization of the collapse based on our August 2019 marine hydroacoustic survey (cf. Hunt et al., 2020), field observations and new interpretations of high-resolution satellite imagery.

Based on our improved knowledge/understanding of subaerial and submarine data, from which we better constrained the geometry and magnitude of the landslide mechanism, we also improved on previous interpretations of the primary landslide scar, which bisected the Anak Krakatau edifice, cutting behind the central vent and removing 50% of its subaerial volume. From our new combined subaerial and marine data sets we also provide a better validated estimate of the landslide failure volume, which lies within a range of 0.175 to 0.272 km^3, with a preferred scenario of 0.224 km^3. This volume is supported by our estimates of the actual landslide deposit volume mapped in the basin to the SW of AK, which is comprised of a main volume of 0.214 ± 0.036 km^3, with a much smaller volume (0.022 ± 0.006 km^3) secondary debris flow. From our new minimum and maximum bounds of the landslide failure surface and geometry, we defined 4 collapse scenario geometries, with volumes between 0.175 and 0.313 km^3.

Observations of a single tsunami wave train, with no subsequently generated waves, are consistent with our interpretation of landslide failure, in a rapid, single phase *en masse* movement, rather than a more piecemeal process; this single event interpretation is also supported by seismic data. In the context of the uncertainty in field observations, all our scenarios successfully reproduced the near- and far-field tsunami flow depth and runup observed in all post-event field survey results published to date, as well as arrival times and time series of surface elevations at tide gauges, and eyewitness reports. This match between our model results and field observations

Commented [TDR14]: Need to clarify that this is the evacuated volume

Commented [sw15]: As above, I think these need correcting in Hunt et al. to correspond to the value stated below shows that our estimated landslide volume range and material rheologies are appropriate to the collapse event.

Despite an observed moderate sensitivity of tsunami impact to the range of modeled landslide sources, particularly in the far-field, the granular rheology appears to yield slide deposits in better agreement with the marine deposits mapped in the 2019 survey (both location and thickness). Additionally, near-field runups are also better predicted using a granular rheology. Regarding the collapse volume, the likeliest value inferred from the 2019 field survey, together with a refined analysis of satellite images, is 0.224 km^3 (referred to in this paper as our preferred scenario), which appears to provide the overall best agreement with the near-field runup measurements, as well as the far-field data. Hence, while the volume is harder to constrain using far-field data, we conclude that tsunami modeling supports the likeliest scenario inferred from the 2019 marine geology survey, although the constraint is weaker than for the rheology.

The AK event highlights the significant hazard posed by relatively small-scale lateral volcanic collapses, which occur *en-masse*, without any precursory signals, and are an efficient and unpredictable tsunami source. Our successful simulations demonstrate that current numerical models can accurately forecast tsunami hazards from these events, even assuming a large uncertainty on the source parameters (e.g., collapse failure plane and volume); this is why the precursor work of Giachetti et al. (2012) provided a reasonable forecast of the event that took place at AK in 2018. In cases such as Anak Krakatau's, the absence of precursory warning signals together with the short travel time following tsunami initiation present a major challenge for mitigating tsunami coastal impact, stressing the need to install early warning systems. In their recent work on AK, Mulia et al. (2020) suggested that a high frequency (HF) radar could have been useful in providing an early detection of the tsunami generated by AK's collapse. In fact, Grilli et al. (2016, 2017a) proposed new algorithms for processing HF radar data to efficiently detect tsunami signals; by performing modeling similar to that reported here, they demonstrated that their algorithm could provide an early detection of landslide tsunamis. Guérin et al. (2018) later applied the method to detect a large meteo-tsunami/surge in actual HF radar data, off of Toffino, BC.

Finally, an important physical aspect not included in NHWAVE is slide dilation, which results from water being sucked into the granular material during slide motion. While this effect could affect tsunami generation, the good agreement observed in the near-field between the measured and predicted runups would indicate that this was not significant during AK's event. Additionally, the many large blocks seen in the debris deposits would indicate that the amount of interstitial water may have been smaller than assumed in simulations and actual dilation effects were small. Nevertheless dilation would be important to include in the model and study in future work.

Commented [SG16]: Added to respond to Simon'scomment

Acknowledgements

STG, CZ and JTK acknowledge support from grants CMMI-1535568 to the University of Rhode Island and CMMI-1537232 to the University of Delaware from the United States (US) National Science Foundation (NSF). Computational resources were provided by University of Delaware Instructional Technology. STG and ARG acknowledge support from NSF grant GEO-17-56665. National Environmental Research Council (NERC) grant NE/S003509/1 is acknowledged by DRT, SW and SE, and Grant NE/T002026/1 by SW, SE and MC. JEH recognizes NERC Urgency Grant NE/T002034/1. DRT, AN and SE publish with permission of the CEO, British Geological Survey. COSMO-SkyMed (CSK) data was provided by the Italian Space Agency through the

Committee on Earth Observation Satellite's Earth Observation (CEOS)'s Volcano Demonstrator (Order ID: 740794). FUNWAVE-TVD is open source software available at http://github.com/fengyanshi/FUNWAVE-TVD/. NHWAVE is open source software available at http://github.com/jimkirby/nhwave/. The Indonesian Ministry of Marine Affairs and Fisheries (http:/tides.big.go.id) is gratefully acknowledged for providing the authors with tide-gauge data, and Dr. Raphael Paris for providing bathymetry/topography data.

References

1. Abadie, S.M., Harris, J.C., Grilli, S.T. & Fabre, R. (2012). Numerical modeling of tsunami waves generated by the flank collapse of the Cumbre Vieja Volcano (La Palma, Canary Islands): Tsunami source and near field effects. Journal of Geophysical Research, vol. 117, pp. C05030, doi:10.1029/2011jc007646.
2. Abadie, S., Paris, A., Ata, R., Le Roy, S., Arnaud, G., Poupardin, A., Clous, L., Heinrich, P., Harris, J., Pedreros, R. and Krien, Y. (2020). La Palma landslide tsunami: calibrated wave source and assessment of impact on French territories. Natural Hazards and Earth System Sciences, vol. 20, no. 11, pp. 3019-3038, doi:10.5194/nhess-20-3019-2020.
3. Abdurrachman, M., Widiyantoro, S., Priadi, B., Ismail, T. (2018). Geochemistry and Structure of Krakatoa Volcano in the Sunda Strait, Indonesia. Geosciences, vol. 8, pp. 111.
4. AGU blog 2019. Anak Krakatau: Planet Labs imagery of the aftermath of the landslide. Accessed Jan. 3, 2019. https://blogs.agu.org/landslideblog/2019/01/03/anak-krakatau-3/?utm_source=AGU+Blogosphere+-+The+Landslide+Blog&utm_campaign=0979aaaa17-RSS_EMAIL_CAMPAIGN_LANDSLIDE&utm_medium=email&utm_term=0_b2461e255e-0979aaaa17-555513653
5. AHA, C. (2018). Indonesia, Tsunami in Sunda Strait.
6. Andersen, O. (2018). Krakatau Volcano: Witnessing the eruption, tsunami and the aftermath 22-23th December 2018, Accessed on December 26, 2018. http://www.oysteinlundandersen.com/krakatau-volcano-witnessing-the-eruption-tsunami-22december2018/.
7. Anon (2018). Global Volcanic Program, in: Venzke, E. (Ed.), Bulletin of the Global Volcanism Network. Smithsonian Institution, Washington.
8. Auker, M.R., Sparks, R.S.J., Siebert, L., Crosweller, H.S., Ewert, J. (2013). A statistical analysis of the global historical volcanic fatalities record. Journal of Applied Volcanology, vol. 2, pp. 1-24, doi:10.1186/2191-5040-2-2.

Commented [SG17]: COmplete

9. Borrero, J.C., T. Solihuddin, H.M. Fritz, P.J. Lynett, G.S. Prasetya, D. Purbani, H.L Salim et al. (2020). Field Survey and Numerical Modelling of the December 22, 2018 Anak Krakatau Tsunami. Pure and Applied Geophys., vol. 177, pp. 2457-2475, doi:10.1007/s00024-020-02515-y
10. Camus, G., Gourgaud, A., Vincent, P.M. (1987). Petrologic evolution of Krakatau (Indonesia): Implications for a future activity. Journal of Volcanology and Geothermal Research, vol. 33, pp. 299-316, doi:10.1016/0377-0273(87)90020-5.
11. Day, S.J., P. Watts, S.T. Grilli and Kirby J.T. (2005). Mechanical Models of the 1975 Kalapana, Hawaii Earthquake and Tsunami. Marine Geology, vol. 215, no. 1-2, pp. 59-92, doi:10.1016/j.margeo.2004.11.008.
12. Day, S. (2015). Volcanic tsunamis, The Encyclopedia of Volcanoes. Elsevier, pp. 993–1009.
13. Day, S., Lanes, P., Silver, E., Hoffmann, G., Ward, S., Driscoll, N. (2015). Submarine landslide deposits of the historical lateral collapse of Ritter Island, Papua New Guinea. Marine and Petroleum Geology, vol. 67, pp. 419-438, doi:10.1016/j.marpetgeo.2015.05.017.
14. Deplus, C., S. Bonvalot, D. Dahrin, M. Diament, H. Harjono, and J. Dubois (1995). Inner structure of the Krakatau volcanic complex (Indonesia) from gravity and bathymetry data. J. Volcan. Geotherm. Res., vol. 64, no. 1-2, pp. 23-52, doi:10.1016/0377-0273(94)00038-I.
15. Dogan, G.G., Annunziato, A., Hidayat, R., Husrin, S., Prasetya, G., Kongko, W., Zaytsev, A., Pelinovsky, E., Imamura, F. and Yalciner, A.C. (2021). Numerical Simulations of December 22, 2018 Anak Krakatau Tsunami and Examination of Possible Submarine Landslide Scenarios. Pure and Applied Geophysics, pp.1-20, doi:10.1007/s00024-020-02641-7.
16. Dunbar, R. I. (1993). Coevolution of neocortical size, group size and language in humans. Behavioral and brain sciences, vol. 16, no. 4, pp. 681-694.
17. Fritz et 16 alii (2019). The 2018 Anak Krakatau tsunami: Near-source field survey on Islands in the Sunda Strait. Presentation at Intl. Symp. on the Lessons Learnt from the 2018 Tsunamis in Palu and Sunda Strait, 26-28 September 2019, Auditorium BMKG, Jakarta – Indonesia.

18. Fornaciai, A., Favalli, M. and Nannipieri, L. (2019). Numerical simulation of the tsunamis generated by the Sciara del Fuoco landslides (Stromboli Island, Italy). Scientific reports, vol. 9, no. 1, pp. 1-12, doi: 10.1038/s41598-019-54949-7.
19. Giachetti, T., Paris, R., Kelfoun, K., Pérez-Torrado, F.J. (2011). Numerical modelling of the tsunami triggered by the Güìmar debris avalanche, Tenerife (Canary Islands): Comparison with field-based data. Marine Geology, vol. 284, pp. 189-202, doi:10.1016/j.margeo.2011.03.018.
20. Giachetti, T., Paris, R., Kelfoun, K., Ontowirjo, B. (2012). Tsunami hazard related to a flank collapse of Anak Krakatau Volcano, Sunda Strait, Indonesia. Geological Society, London, Special Publications, vol. 361, pp. 79-90.
21. Glimsdal, S., Pedersen, G. K., Harbitz, C. B., and Løvholt, F. (2013). Dispersion of tsunamis: does it really matter? Natural hazards and earth system sciences, vol. 13, no. 6, pp. 1507-1526, doi: 10.5194/nhess-13-1507-2013.
22. Gouhier, M. and Paris, R (2019). SO2 and tephra emissions during the December 22, 2018 Anak Krakatau eruption. Volcanica, vol. 2, no. 2, pp. 91-103, doi: 10.30909/vol.02.02.91103.
23. Grilli, S.T., Ioualalen, M, Asavanant, J., Shi, F., Kirby, J. and Watts, P. (2007). Source Constraints and Model Simulation of the December 26, 2004 Indian Ocean Tsunami. Journal of Waterway Port Coastal and Ocean Engineering, vol. 133, no. 6, pp. 414-428, doi:10.1061/(ASCE)0733-950X(2007)133:6(414).
24. Grilli, S.T. J.C. Harris, T. Tajalibakhsh, T.L. Masterlark, C. Kyriakopoulos, J.T. Kirby and F. Shi (2013). Numerical simulation of the 2011 Tohoku tsunami based on a new transient fem co-seismic source: Comparison to far- and near-field observations. Pure and Applied Geophysics, vol. 170, pp. 1333–1359, doi:10.1007/s00024-012-0528-y.
25. Grilli, S.T., O'Reilly, C., Harris, J.C., Tajelli-Bakhsh, T., Tehranirad, B., Banihashemi, S., Kirby, J.T., Baxter, C.D.P., Eggeling, T., Ma, G., and F. Shi (2015). Modeling of SMF tsunami hazard along the

upper US East Coast: detailed impact around Ocean City, MD. Natural Hazards, vol. 76, pp. 705-746; doi:10.1007/s11069-014-1522-8.

26. Grilli, S.T., Grosdidier S. and C.-A. Guérin (2016). Tsunami detection by High Frequency Radar beyond the continental shelf. I. Algorithms and validation on idealized case studies. Pure and Applied Geophysics, vol. 173, no. 12, pp. 3,895-3,934, doi:10.1007/s00024-015-1193-8

27. Grilli, S.T., Guérin, C.-A., Shelby, M., Grilli, A., P. Moran, Grosdidier, S. and T.L. Insua (2017a). Tsunami detection by High Frequency Radar beyond the continental shelf: II. Extension of algorithms and validation on realistic case studies. Pure and Appl. Geophys., vol. 174, no. 1, pp. 3,003-3,028, doi:10.1007/s00024-017-1619-6.

28. Grilli, S.T., Shelby, M., Kimmoun, O., Dupont, G., Nicolsky, D., Ma, G., Kirby, J.T. and F. Shi (2017b). Modeling coastal tsunami hazard from submarine mass failures: effect of slide rheology, experimental validation, and case studies off the US East coast. Natural Hazards, vol. 86(1), pp. 353-391, doi:10.1007/s11069-016-2692-3.

29. Grilli, S.T., Tappin, D.R., Carey, S., Watt, S.F.L., Ward, S.N., Grilli, A.R., Engwell, S.L., Zhang, C., Kirby, J.T., Schambach, L., Muin, M. (2019). Modelling of the tsunami from the December 22, 2018 lateral collapse of Anak Krakatau volcano in the Sunda Straits, Indonesia. Scientific Reports, vol. 9, no. 11946, doi:10.1038/s41598-019-48327-6.

30. Guérin C.-A., S.T. Grilli, P. Moran, A.R. Grilli, T.L. Insua (2018). Tsunami detection by High Frequency Radar in British Columbia: performance assessment of the Time-Correlation Algorithm for synthetic and real events. Ocean Dynamics, 68(4-5), pp. 423-438, doi:10.1007/s10236-018-1139-7.

31. Gurney, J. (2018) Low frequency analysis of the 13:55 event (arrival at Bungbulang at 13:57 UTC), UK Earthquake Bulletin.

32. Heidarzadeh, M., Ishibe, T., Sandanbata, O., Muhari, A., Wijanarto, A.B. (2020). Numerical modeling of the subaerial landslide source of the 22 December 2018 Anak Krakatoa volcanic tsunami, Indonesia. Ocean Engineering, vol. 195, no. 106733.

33. Heidarzadeh, M., Putra, P. S., Nugroho, S. H., and Rashid, D. B. Z. (2020). Field survey of tsunami heights and runups following the 22 December 2018 Anak Krakatau volcano tsunami, Indonesia. Pure and Applied Geophysics, vol. 177, no. 10, pp. 4577-4595, doi: 10.1016/j.oceaneng.2019.106733
34. Hunt, J.E., Wynn, R.B., Masson, D.G., Talling, P.J., Teagle, D.A.H. (2011). Sedimentological and geochemical evidence for multistage failure of volcanic island landslides: A case study from Icod landslide on north Tenerife, Canary Islands. Geochem. Geophys. Geosyst., vol. 12, no. Q12007, doi: 10.1029/2011GC003740
35. Hunt, J.E., Tappin, D.R., Watt, S.F., Susilohadi, S., Novellino, A., Ebmeier, S.K., Cassidy, M., Engwell, S.L., Grilli, S.T., Hanif, M., Priyanto, W.S., Clare, M.A., Abdurrachman, M., Udrekh, U. (2020). Submarine landslide megablocks show half the island of Anak Krakatau failed on December 22nd, 2018. Nature Communication (in revisions).
36. Imamura, F. and Imteaz, M.M.A. (1995). Long waves in two-layers: Governing equations and numerical model. Science of Tsunami Hazards, vol. 13, no. 1, pp. 3-24.
37. Ina-COAP (2019). *Tide Gauge data in Indonesia*, http://tides.big.go.id/las/UI.vm Accessed Jan. 3, 2019.
38. Ioualalen, M., Asavanant, J., Kaewbanjak, N., Grilli, S.T., Kirby, J.T. and P. Watts (2007). Modeling the 26th December 2004 Indian Ocean tsunami: Case study of impact in Thailand. Journal of Geophysical Research, vol. 112, pp. C07024, doi:10.1029/2006JC003850.
39. Johnson, R.W., (1987). Large-scale volcanic cone collapse: the 1888 slope failure of Ritter Volcano, and other examples from Papua New Guinea. Bulletin of Volcanology, vol. 49, pp. 669–679, doi: 10.1007/BF01080358.
40. Kirby, J.T., Shi, F., Tehranirad, B., Harris, J.C. and Grilli, S.T. (2013). Dispersive tsunami waves in the ocean: Model equations and sensitivity to dispersion and Coriolis effects. Ocean Modeling, vol. 62, pp. 39-55, doi:10.1016/j.ocemod.2012.11.009.

41. Kirby, J.T., Shi, F., Nicolsky, D., and S. Misra (2016). The 27 April 1975 Kitimat, British Colombia, submarine landslide tsunami: a comparison of modeling approaches. Landslides, vol. 13, no. 6, pp. 1421-1434; doi: 10.1007/s10346-016-0682-x.

42. Løvholt, F., Pedersen, G., Gisler, G. (2008). Oceanic propagation of a potential tsunami from the La Palma Island. Journal of Geophysical Research, vol. 113, no. C09026, doi:10.1029/2007JC004603.

43. Ma, G., Shi, F., and Kirby, J.T. (2012). Shock-capturing non-hydrostatic model for fully dispersive surface wave processes. Ocean Modelling, vol. 43-44, pp. 22-35, doi:10.1016/j.ocemod.2011.12.002.

44. Ma, G., Kirby, J.T., Hsu, T.J., and Shi, F. (2015). A two-layer granular landslide model for tsunami wave generation: theory and computation. Ocean Modelling, vol. 93, pp. 40-55, doi:10.1016/j.ocemod.2015.07.012.

45. Muhari, A. (2018). in *Kompas*, (in Indonesian) https://sains.kompas.com/read/2018/12/23/180319123/menyoal-dakwaan-pada-anak-krakatau-tentang-kasus-tsunami-selat-sunda?page=all. Acessed Dec. 23, 2018.

46. Muhari, A., Heidarzadeh, M., Susmoro, H., Nugroho, H.D., Kriswati, E., Wijanarto, A.B., Imamura, F. and Arikawa, T. (2019). The December 2018 Anak Krakatau volcano tsunami as inferred from post-tsunami field surveys and spectral analysis. Pure and Applied Geophysics, vol. 176, no. 12, pp. 5219-5233, doi: https:10.1007/s00024-019-02358-2.

47. Mulia, I.E., Watada, S., Ho, T.-C., Satake, K., Wang, Y., Aditiya, A. (2020). Simulation of the 2018 Tsunami Due to the Flank Failure of Anak Krakatau Volcano and Implication for Future Observing Systems. Geophysical Research Letters, vol. 47, no. e2020GL087334, doi:10.1029/2020GL087334.

48. Novellino, A., Engwell, S.L., Grebby, S., Day, S., Cassidy, M., Madden-Nadeau, A., Watt, S., Pyle, D., Abdurrachman, M., Edo Marshal Nurshal, M. and Tappin, D.R. (2020). Mapping recent shoreline changes spanning the lateral collapse of Anak Krakatau Volcano, Indonesia. Appl. Sci., vol. 10, no. 2, pp. 536, doi: 10.3390/app10020536.

49. Omira, R. and Ramalho, I. (2020). Evidence-Calibrated Numerical Model of December 22, 2018, Anak Krakatau Flank Collapse and Tsunami. Pure and Applied Geophysics, vol. 177, no. 7, pp. 3059-3071, doi: 10.1007/s00024-020-02532-x.

50. Paris, R. (2015). Source mechanisms of volcanic tsunamis. Philosophical Transactions of the Royal Society of London A: Mathematical, Physical and Engineering Sciences, vol. 373, no. 2053, pp. 20140380, doi: 10.1098/rsta.2014.0380.

51. Paris, A., Heinrich, P., Paris, R., and Abadie, S. (2020a). The December 22, 2018 Anak Krakatau, Indonesia, landslide and tsunami: preliminary modeling results. Pure and Applied Geophysics, vol. 177, no. 2, pp. 571-590, doi: 10.1007/s00024-019-02394-y

52. Paris, R., Goto, K., Goff, J. and Yanagisawa, H. (2020b). Advances in the study of mega-tsunamis in the geological record. Earth-Science Reviews, no. 103381, doi:10.1016/j.earscirev.2020.103381.

53. Perttu, A., Caudron, C., Assink, J.D., Metz, D., Tailpied, D., Perttu, B., Hibert, C., Nurfiani, D., Pilger, C., Muzli, M. and Fee, D. (2020). Reconstruction of the 2018 tsunamigenic flank collapse and eruptive activity at Anak Krakatau based on eyewitness reports, seismo-acoustic and satellite observations. Earth and Planetary Science Letters, vol. 541, pp.116268, doi: 10.1016/j.epsl.2020.116268.

54. Putra, P. S., Aswan, A., Maryunani, K. A., Yulianto, E., Nugroho, S. H., & Setiawan, V. (2020). Post-Event Field Survey of the 22 December 2018 Anak Krakatau Tsunami. Pure and Applied Geophysics, vol. 177, pp. 2477–2492, doi:10.1007/s00024-020-02446-8

55. PVMBG (2018). Activity reports for Anak Krakatau from 01/12/2018 – 03/01/2019. Pusat Vulkanologi dan Mitigasi Bencana Geologi.

56. Priyanto, W.S., Hunt, J.E., Hanif, M., Tappin, D.R., Permana, H., Susilohadi, S., Cassidy, M. and Yulianto, E. (2020). Bathymetry and Shallow Seismic Imaging of the 2018 Flank Collapse of Anak Krakatau. Frontiers in Earth Science, 8, pp. 649, doi:10.3389/feart.2020.577448.

57. Ren, Z., Wang, Y., Wang, P., Hou, J., Gao, Y., and Zhao, L. (2020). Numerical study of the triggering mechanism of the 2018 Anak Krakatau tsunami: eruption or collapsed landslide?. Natural Hazards, vol. 102, no. 1, pp. 1-13, doi:10.1007/s11069-020-03907-y.

58. Reynolds, J. (2019). *Post-collapse image of Anak Krakatau. Earth Uncut TV*, https://twitter.com/hashtag/Krakatau?src=hash, Accessed Jan. 11, 2019.

59. Schambach L., Grilli S.T., Kirby J.T. and F. Shi (2019). Landslide tsunami hazard along the upper US East Coast: effects of slide rheology, bottom friction, and frequency dispersion. Pure and Applied Geophys*ics*, vol. 176, no. 7, pp. 3,059-3,098, doi.org/10.1007/s00024-018-1978-7.

60. Schambach L., Grilli S.T., Tappin D.R., Gangemi M.D., and G. Barbaro (2020a). New simulations and understanding of the 1908 Messina tsunami for a dual seismic and deep submarine mass failure source, *Marine Geology*, vol. 421, pp. 106093, doi: 10.1016/j.margeo.2019.106093.

61. Schambach L., Grilli S.T. and D.R. Tappin (2020b). New high-resolution modeling of the 2018 Palu tsunami, based on supershear earthquake mechanisms and mapped coastal landslides, supports a dual source. Frontiers in Earth Sciences, vol. 8, pp. 627, doi:10.3389/feart.2020.598839.

62. Simkin, T., Fiske, R.S. (1983). Krakatau 1883: the volcanic eruption and its effects. Smithsonian Institution Press, Washington, D.C.

63. Siswowidjoyo, S. (1983). Krakatau, Symposium on 100 years development Krakatau its surroundings. Indonesian Inst. Sci. Jakarta, Jakarta, pp. 191–198.

64. Shi, F., Kirby, J.T., Harris, J.C., Geiman, J.D. and S.T. Grilli (2012). A high-order adaptive time-stepping TVD solver for Boussinesq modelling of breaking waves and coastal inundation. Ocean Modelling, vol. 43-44, pp. 36-51, doi:10.1016/j.ocemod.2011.12.004.

65. Stehn, C. (1929). The geology and volcanism of the Krakatau group, Krakatau, Proc. 4th Pacific Sci. Congr, Batavia I, pp. 1-55.

66. Tappin, D.R., Watts, P., Grilli, S.T. 2008. The Papua New Guinea tsunami of 1998: anatomy of a catastrophic event. Natural Hazards and Earth System Sciences, vol. 8, pp. 243-266, doi:www.nat-hazards-earth-syst-sci.net/8/243/2008/

67. Tappin, D.R., Grilli, S.T., Harris, J.C., Geller, R.J., Masterlark, T., Kirby, J.T., Shi, F., Ma, G., Thingbaijam, K.K.S., and P.M. Mai (2014). Did a submarine landslide contribute to the 2011 Tohoku tsunami? Marine Geology, vol. 357, pp. 344-361, doi:10.1016/j.margeo.2014.09.043.
68. TDMRC (Tsunami, D., and Mitigation, Research, Center) (2019). Post Sunda Strait Tsunami Survey. Tsunami, Disaster, and Mitigation, Research, Center, Jakarta.
69. Tehranirad B., Harris J.C., Grilli A.R., Grilli S.T., Abadie S., Kirby J.T. and F. Shi 2015. Far-field tsunami impact in the north Atlantic basin from large scale flank collapses of the Cumbre Vieja volcano, La Palma. Pure and Applied Geophysics, vol. 172, no. 12, pp. 3,589-3,616, doi:10.1007/s00024-015-1135-5.
70. Tinti, S., Bortolucci, E. and Romagnoli, C. (2000). Computer simulations of tsunamis due to sector collapse at Stromboli, Italy. Journal of Volcanology and Geothermal Res., vol. 96, pp. 103-128, doi:10.1016/S0377-0273(99)00138-9.
71. Umbgrove, J. H. F. (1928). The first days of the new submarine volcano near Krakatoa. Leidse Geologische Mededelingen, vol. 2, no. 1, pp. 325-328.
72. Verbeek, R.D.M. (1885). Krakatau. Government Press Batavia.
73. Verbeek, R.D.M. (1983). Krakatau, in: Simkin, T., Fiske, R.S. (Eds.), Krakatau 1883: The Volcanic Eruption and its Effects. Smithsonian Press, Washington, D.C., pp. 169-277.
74. Ward, S.N., Day, S. (2001). Cumbre Vieja volcano – Potential collapse and tsunami at La Palma, Canary Islands. Geophysical Research Letters, vol. 28, no. 17, pp. 3397– 3400, doi: 10.1029/2001GL013110.
75. Ward, S.N. and Day, S. (2003). Ritter Island Volcano-lateral collapse and the tsunami of 1888. Geophysical Journal International, vol. 154, pp. 891–902, doi: 10.1046/j.1365-246X.2003.02016.x.
76. Ward, S. N. and Day, S. (2006). Particulate kinematic simulations of debris avalanches: interpretation of deposits and landslide seismic signals of Mount Saint Helens, 1980 May 18. Geophysical Journal International, vol. 167, no. 2, pp. 991-1004.

77. Watt, S.F.L., Karstens, J., Micallef, A., Berndt, C., Urlaub, M., Ray, M., Desai, A., Sammartini, M., Klaucke, I., Böttner, C., Day, S., Downes, H., Kühn, M., Elger, J. (2019). From catastrophic collapse to multi-phase deposition: Flow transformation, seafloor interaction and triggered eruption following a volcanic-island landslide. Earth and Planetary Science Letters, vol. 517, pp. 135-147, doi: 10.1016/j.epsl.2019.04.024.

78. Williams, R., Rowley, P. and Garthwaite, M.C. (2019). Reconstructing the Anak Krakatau flank collapse that caused the December 2018 Indonesian tsunami. Geology, vol. 47, no. 10, pp. 973-976, doi: 10.1130/G46517.1**.**

79. Yavari-Ramshe, S., and Ataie-Ashtiani, B. (2016). Numerical simulation of subaerial and submarine landslide generated tsunami waves—recent advances and future challenges. Landslides, 13(6), pp. 1325–1368, doi: 10.1007/s10346-016-0734-2.

80. Ye, L., Kanamori, H., Rivera, L., Lay, T., Zhou, Y., Sianipar, D., and Satake, K. (2020). The 22 December 2018 tsunami from flank collapse of Anak Krakatau volcano during eruption. Sci. Advances, vol. 6, no. 3, pp. eaaz1377, doi:10.1126/sciadv.aaz1377.

81. Zengaffinen, T., Løvholt, F., Pedersen, G.K., Muhari, A. (2020). Modelling 2018 Anak Krakatoa Flank Collapse and Tsunami: Effect of Landslide Failure Mechanism and Dynamics on Tsunami Generation. Pure and Applied Geophysics, vol. 177, pp. 2493-2516, doi: 10.1007/s00024-020-02489-x.

82. Zhang C., Kirby J., Shi F., Ma G. and S.T. Grilli (2021a). A two-layer non-hydrostatic landslide model for tsunami generation on irregular bathymetry. 1. Theoretical basis. *Ocean Modelling*, 101749 doi:10.1016/j.ocemod.2020.101749.

83. Zhang C., Kirby J., Shi F., Ma G. and S.T. Grilli (2021b). A two-layer non-hydrostatic landslide model for tsunami generation on irregular bathymetry. 2. Numerical discretization and model validation. *Ocean Modelling* (minor revisions).

Tables

Grid	Mesh size (N, M)	Resolution (m)	SW Corner (Lat., Lon.)
G1	3680,3900	50	-7°, 104.4°
G2	955, 1155	30 (horiz.) 7 σ (vert.)	-6.2357°, 105.2916°

Table 1: Parameters of grids used in simulations with NHWAVE (G2) and FUNWAVE (G1) (Fig. 1).

WG	Lon E. (Deg.)	Lat N. (Deg.)	Depth (m)	*t* meas. crest (s)	*t* meas. 1 cm (s)	*t* sim. crest (s)	*t* sim. 1 cm (s)
1.	105.4066^o	-6.1234^o	239.50	N/A	N/A	53-65	15.6-24.2
2.	105.3733^o	-6.1524^o	88.22	N/A	N/A	165.1-175.5	118.0-127.0
3.	105.4246^o	-6.0691^o	49.32	N/A	N/A	179-191	131.2-140.0
4.	105.4954^o	-6.1279^o	58.50	N/A	N/A	244.5-254.5	197.5-208.0
5.	105.3571^o	-6.1361^o	90.74	N/A	N/A	188.5-190.4	165.5-169.4
6.	105^o 50’ 15.0”	-6^o 11’ 21.5”	4.70	1980	1923	1995-2006	1967-1979
7.	105^o 57’ 10.8”	-6^o 01’ 02.5”	3.64	2700	2587	2712-2727	2617-2629
8.	104^o 37’ 08.5”	-5^o 30’ 01.2”	3.67	2520	2292	2550-2568	2358-2382
9.	105^o 19’ 06.1”	-5^o 28’ 08.7”	3.92	3600	3390	3660-3678	3564-3624

Table 2: Parameters of numerical wave gauges (WG) 1-9 (Figs. 1a,b): Lat-Lon, depth (in grids G1 (6-9) and G2 (1-5), assuming a MWL = MSL + 1.5 m, corresponding to the estimated average tide elevation at the time of the event), and arrival time (1 cm elevation or first main crest), measured/simulated range for 8 scenarios (Figs. 6,7). WG 1-5 have no measured time (Fig. 6), but WG 6-9 are collocated with Tide Gauges (Fig. 10) at: (5) Serang, Marina Jambu, (6) Ciwandan, (8) Kota-Angung, (9) Panjang. In simulations, AK collapse is assumed to take place at 20:57’ local time (UTC + 7). Simulated crest arrival time ranges at 9 WG for 8 scenarios are within 2-18 s. Simulated differences in crest arrival time at tide gauges are 15-78 s, compared to the 1 min data sampling interval. N/A: Not Applicable.

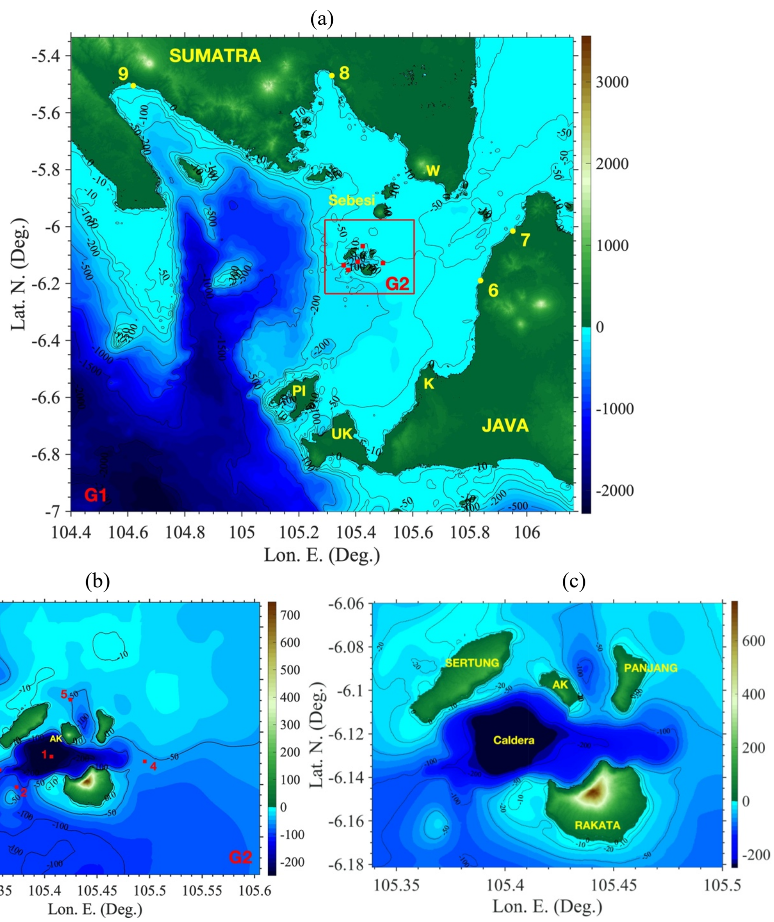

Figure 1: (a) Study area covered by 2D FUNWAVE 50 m Cartesian grid G1; (b) zoom-in onto 3D NHWAVE 30 m Cartesian gird grid G2 (red box in (a)), with 7 vertical σ layers, encompassing Anak-Krakatau (AK) and its surrounding islands (Rakata, Sertung, Panjang). Numbered symbols mark locations of numerical wave gauges (6-9 are collocated with tide gauges). Black contours and color scale is (a,b) pre- and (c) post-collapse (likeliest scenario) bathymetry/topography in meter, including an observed +1.5 m mean tide level. Letters in (a) are localities: (UK) Ujung Kulon; (K) Kolijaah; (PI) Panaitan Island; (W) Waymuli.

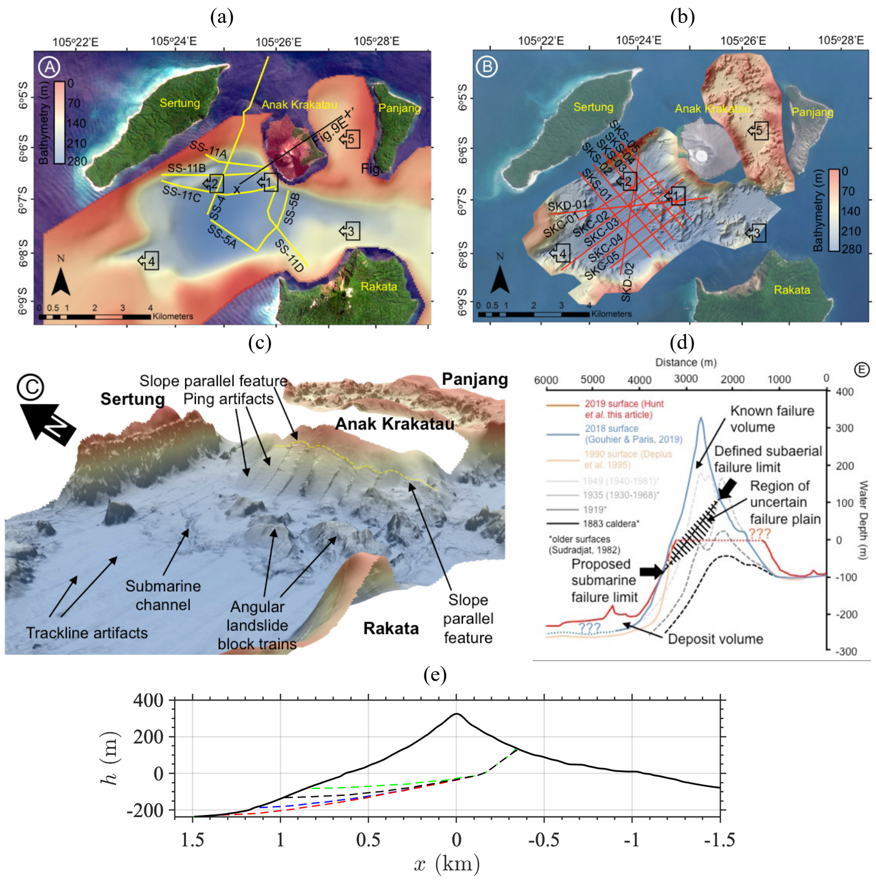

Figure 2: DRAFT! (a,b,c) Pre- and post-collapse bathymetry/topography of AK and surrounding islands (Fig 1): (a) 1990 pre-collapse bathymetry with locations of 2017 seismic reflection profiles; (b) post-collapse bathymetry from August 2019 showing landslide deposits and traces of collected seismic reflection profiles survey (Hunt et al., 2020); and c) rendering of (b) bathymetry showing large, blocky landslide deposits at the base of AK's SW flank. (d) AK historical profiles in SW transects, compared to August 2019 field survey (Hunt et al., 2020) with proposed failure surface with uncertainty region. (e) pre-collapse AK profile (SW direction, 225 deg. To N) used in simulations (no vertical exaggeration), with traces (dashed lines) of 4 failure surface scenarios modeled with NHWAVE, of total collapse volume: (red) 0.313; (blue) 0.272; (black) 0.224 (deemed the likeliest scenario; see Figs. 1c and 3b); and (green) 0.175 km^3.

1148

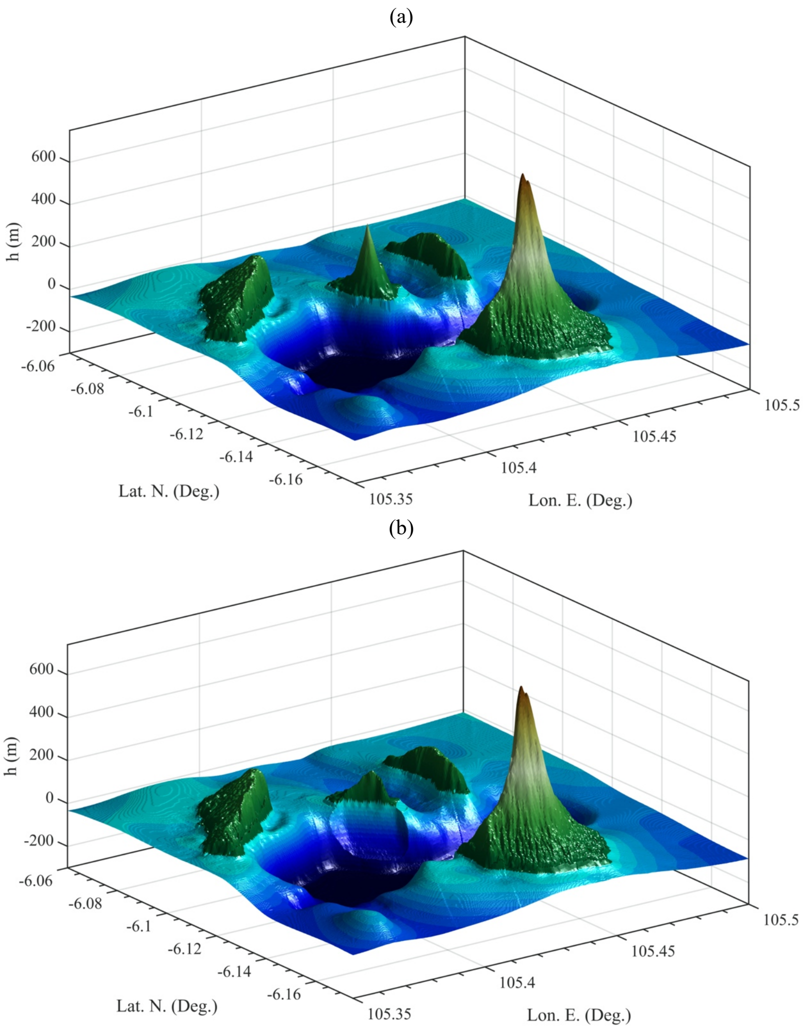

Figure 3: 3D view of composite pre- and post-collapse (likeliest scenario) bathymetry/topography of AK and surrounding islands used in NHWAVE Grid G2 (Fig. 1c footprint), based on available pre-event data outside of Krakatau islands and August 2019 field survey data (see Fig. 2) in the caldera and surrounding islands (Hunt et al., 2020).

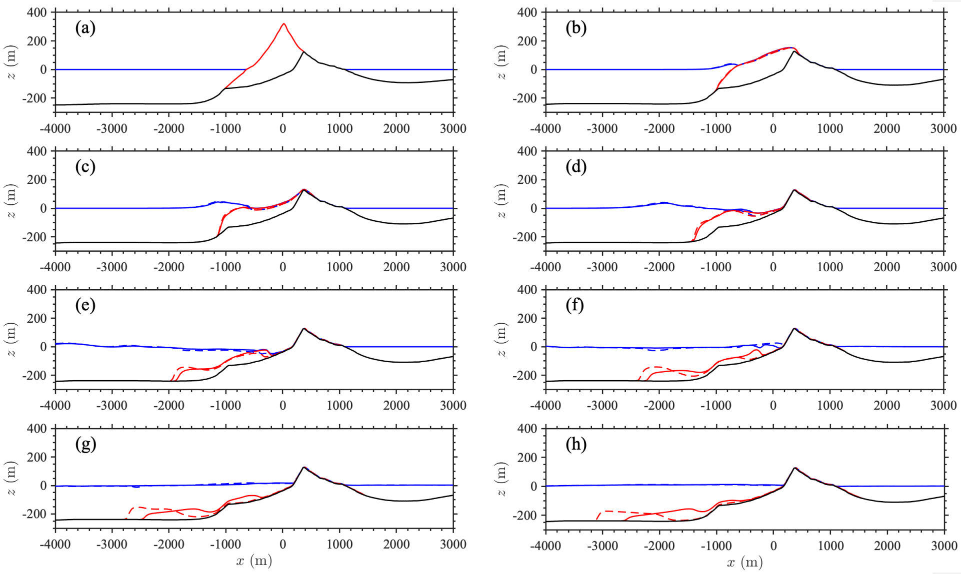

Figure 4: Simulation of likeliest AK collapse volume scenario (0.224 km^3) with NHWAVE in Grid G2 (Fig. 1) with a granular (solid) or viscous (dashed) rheology. Sub-panels show SW (225 deg. to north; Fig. 2) transects of computed instantaneous surface elevations (blue) and slide profiles (red), at t = (a) 0, (b) 10, (c) 20, (d) 40, (e) 80, (f) 120, (g) 160 and (h) 200 s.

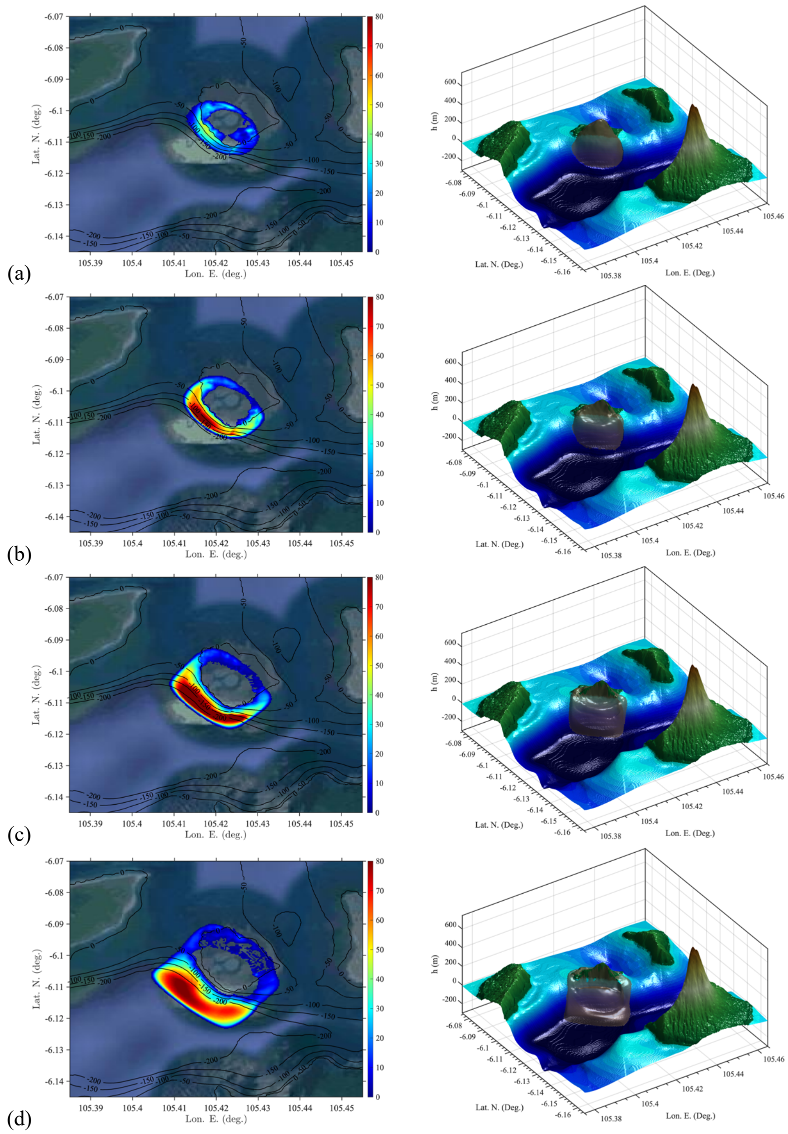

Figure 5: Snapshots of slide motion for granular case of Fig. 4, at t = (a) 10, (b) 20, (c) 40, (d) 80, (e) 120, (f) 160, (g) 200, and (h) 380 s. Color scale is slide thickness in meter. Contours are depth in meter.

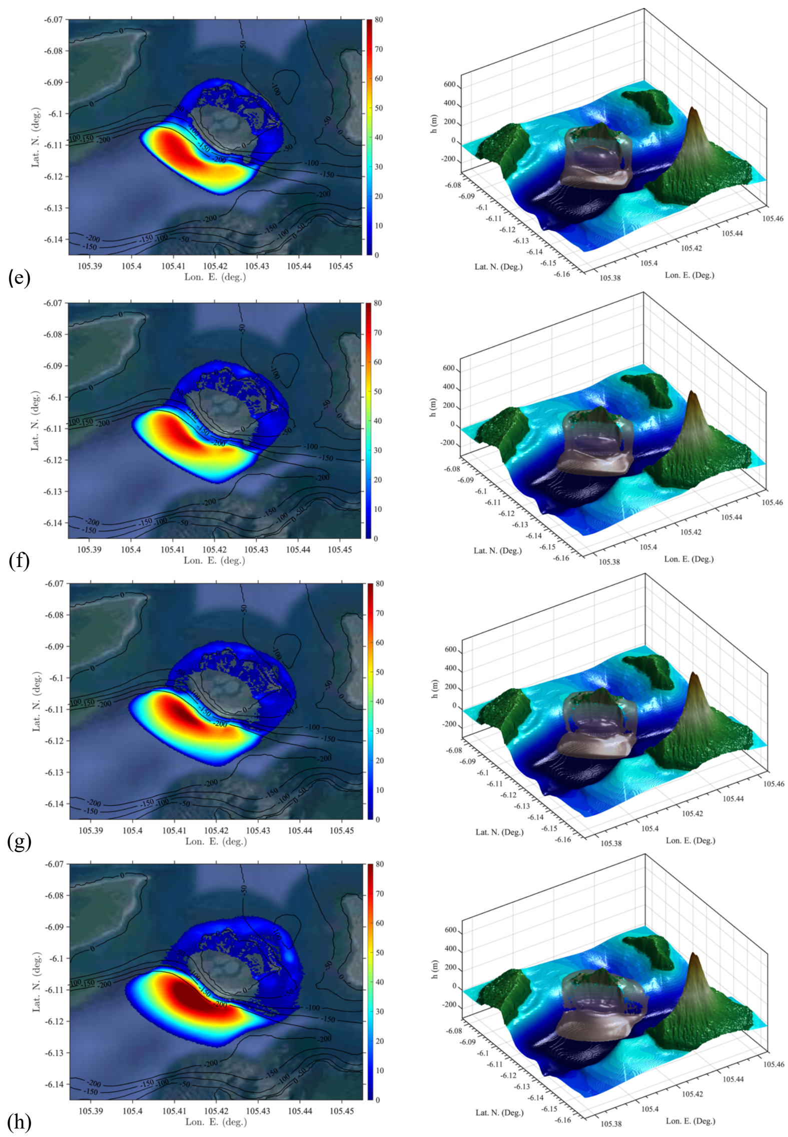

Figure 5: continued.

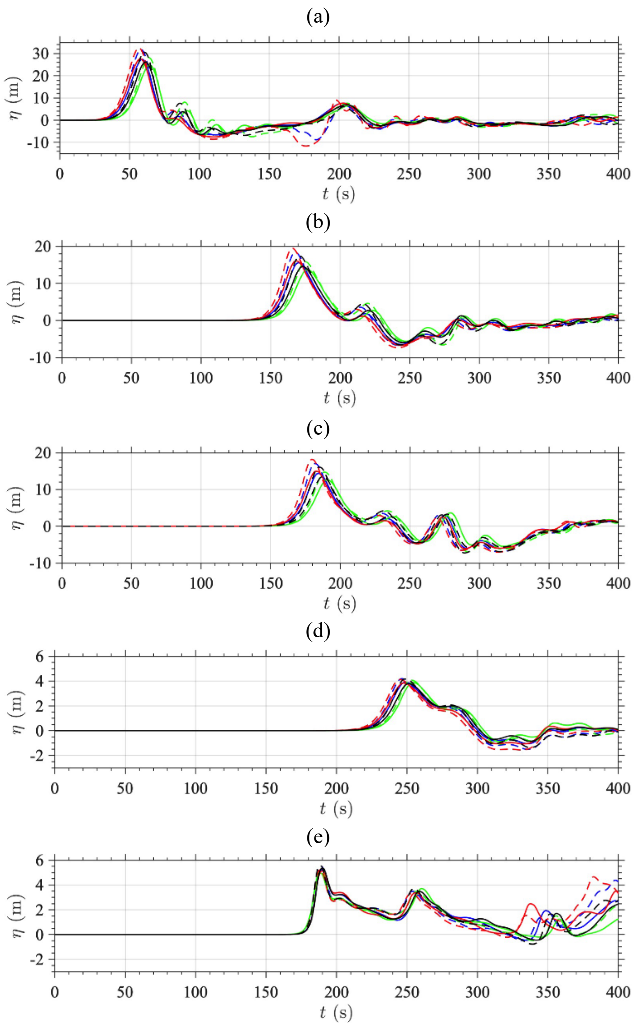

Figure 6: Time series of surface elevations computed at numerical wave gauges (WG) 1-5 (a-e; Fig. 1b) with NHWAVE in Grid G2 (Fig. 1), for 8 AK collapse scenarios with a granular (solid) or viscous (dashed) rheology, and volume (Fig. 2c): (red) 0.313; (blue) 0.272; (black) 0.224 (likeliest scenario; see Figs. 1c and 3b); (green) 0.175 km^3. Time t = 0 is estimated collapse time, 20:57′ local time (UTC + 7). Note, reference level in <u>simulations</u> is MWL = MSL + 1.5 m (tide elevation).

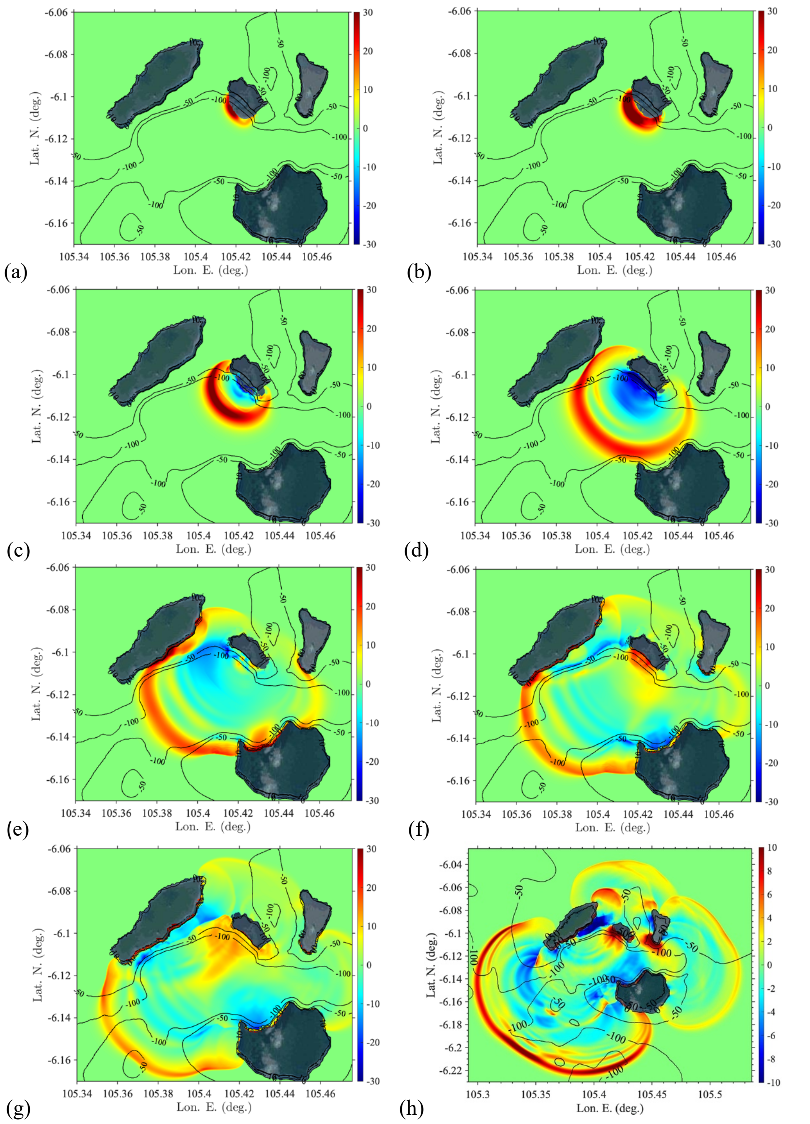

Figure 7: Snapshots of free surface elevations computed with NHWAVE in Grid G2, for likeliest collapse scenario (granular, 0.224 km^3), at t = (a) 10, (b) 20, (c) 40, (d) 80, (e) 120, (f)160, (g) 200, and (h) 380 s (latter time is FUNWAVE initialization). Same case as Fig. 5. Reference level in simulations is MSL + 1.5 m.

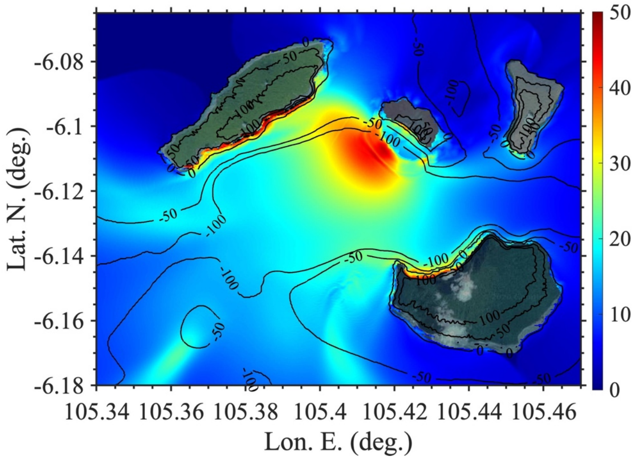

Figure 8: Maximum envelope of surface elevations computed with NHWAVE in Grid G2 for AK collapse likeliest scenario (granular, 0.224 km^3), up to t = 420 s (color scale in meter). Reference level in simulations is MWL = MSL + 1.5 m.

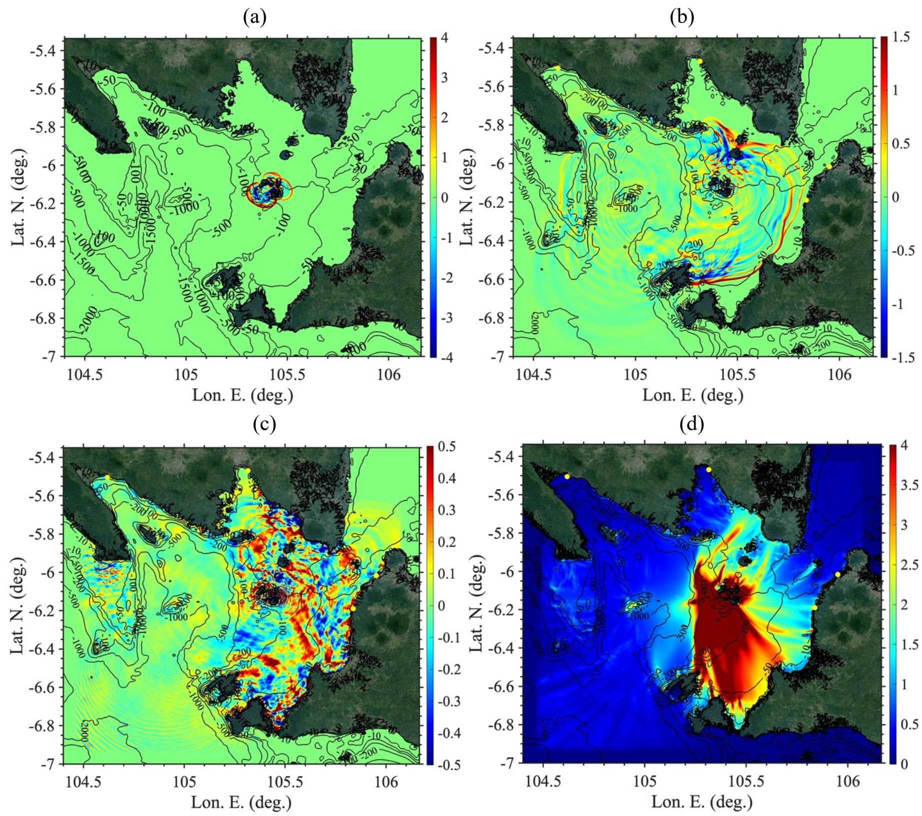

Figure 9: Tsunami surface elevations computed with FUNWAVE in Grid G1 for AK collapse likeliest scenario (granular, 0.224 km^3). Initial elevation at t = (a) 380 s from NHWAVE simulation, (b) 1800 s, and (c) 3600 s; (d) envelope of maximum elevations up to t = 7580 s (different color scales in meter). Maps show topography from Google Earth georeferenced satellite images embedded using an API key. Reference level in simulations is MWL = MSL + 1.5 m. Yellow bullets mark locations of tide gauges (see Fig. 1a).

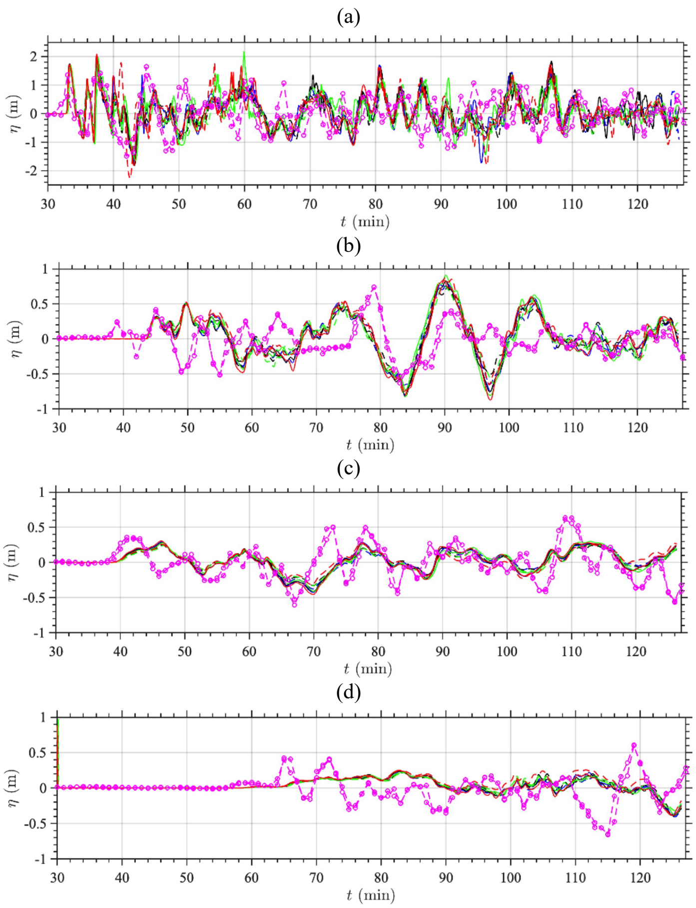

Figure 10: Time series of surface elevations, in simulations with respect to MWL = MSL + 1.5 m, at numerical wave gauges 6-9 (a-d; Fig. 1a), computed with FUNWAVE for 8 AK collapse scenarios with line codes defined as in Fig. 6, compared to collocated detided observations (o) with 2 sensors, at 4 tide gauges (Table 2). Time $t = 0$ is estimated collapse time, 20:57′ local time (UTC + 7).

(a)

(b)

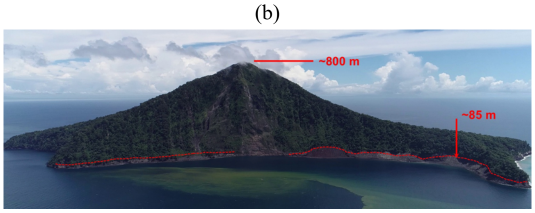

(c)

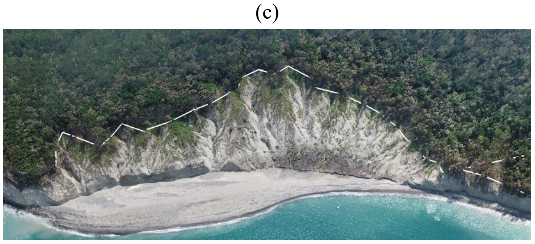

(d)

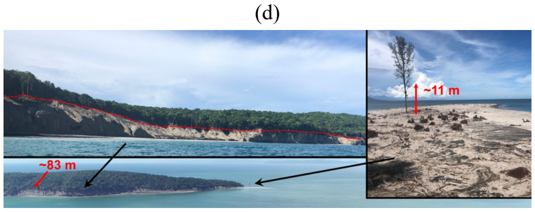

(e)

(e)

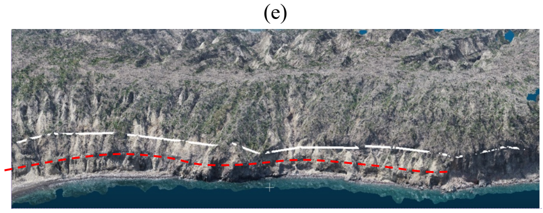

Commented [MEMN18]: what if the wave-impact line is lower as shown with red dashed line (on top of the steepest slope; not on the tree line) so it might match the simulation?

Figure 11: Pictures from AK field surveys of near-field runups: (a,c,e) the authors August 2019 drone survey; (b,d) Borrero's et al. (2020) in 02/2019, with (a/b) Rakata's N/NW shores; (c/d) Sertung's SE/NE shores; and (e) Panjang's W shore (Fig. 1c).

Commented [sw19]: Need a scale on the drone survey images, let me know if you need me to redo any of these.

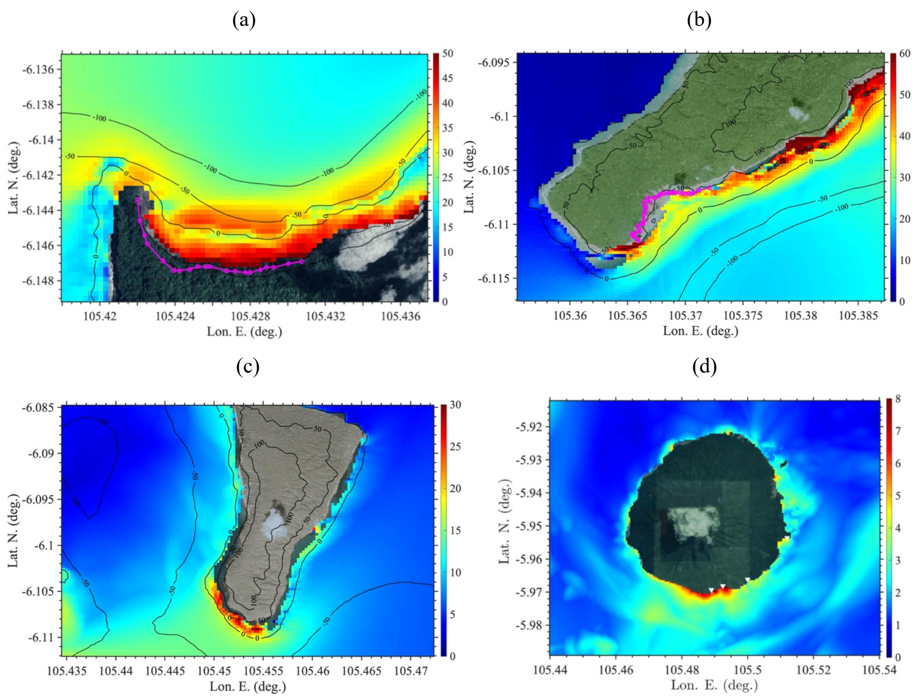

Figure 12: Zoom-in on maximum surface elevation computed with (a-c) NHWAVE in Grid G2 (Fig. 8) or (d) FUNWAVE in Grid G1 (Fig. 9d) for the likeliest collapse scenario (granular, 0.224 km^3), along (Figs. 1a,c): (a) Rakata's NW shore, (b) Sertung's SW shore, (c) Panjang's S shore, and (d) Sebesi. Pink circles/line in (a,b) indicate August 2019 drone survey (Figs. 11a,c); white triangles in (d) are flow depth/runup from Borrero et al.'s (2020) 02/2019 field survey of Sebesi (7.5, 9.0, 2.6, 2.0 m from W to E, respectively, referred here to MWL). Black contours are bathymetry/topography in meter. Note, reference level in simulations is MWL = MSL + 1.5 m (tide elevation).

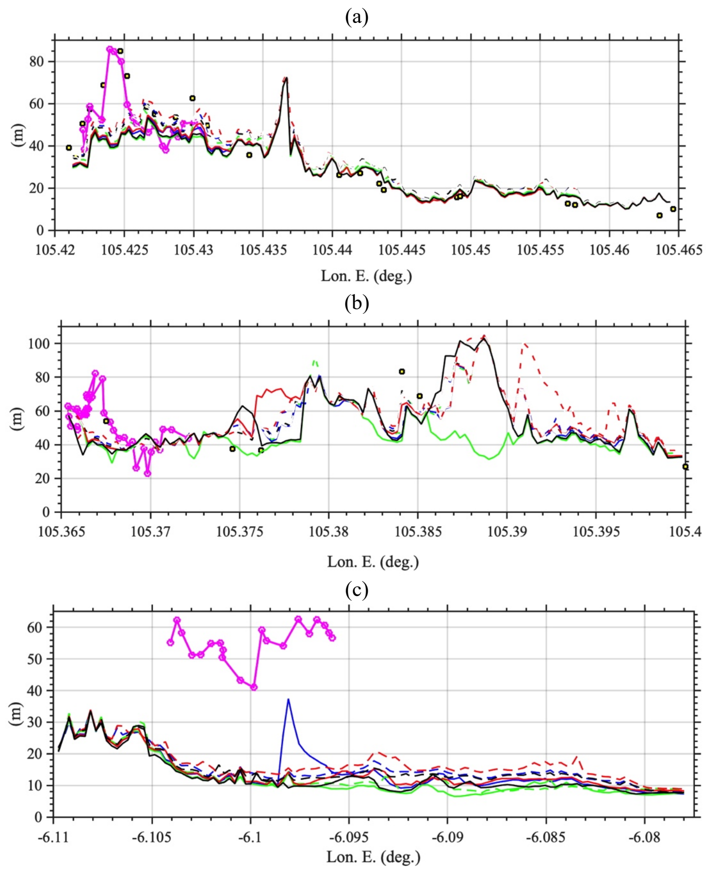

Figure 13: Maximum runup computed with NHWAVE along (Figs. 1c, 11, 12): (a) Rakata's N shore; (b) Sertung's S shore; and (c) Panjang's W shore, for 8 AK collapse scenarios with line codes defined as in Fig. 6, compared to (Fig. 11) the authors August 2019 drone field survey (pink line/circles) of tree line and field measurements (yellow squares) of Borrero et al. (2020); note, the latter authors reported an 8 m flow depth for north of Panjang. Black solid lines denote our preferred volume scenario with granular rheology. Note, in simulations and the field data, zero elevation is MWL = MSL + 1.5 m (tide elevation).

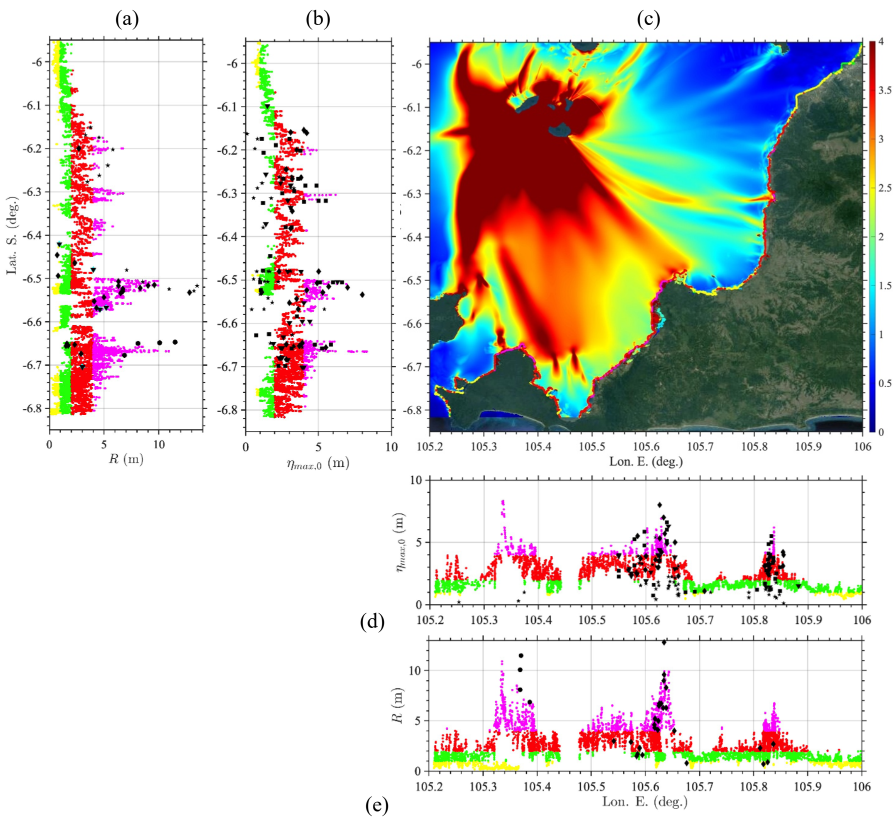

Figure 14: (a,e) Maximum Runup *R*, and (b,d) flow depth at the shore $\eta_{max,0}$ (along 0 m contour) from (a) maximum envelope of surface elevation computed with FUNWAVE in Grid G1, for likeliest AK collapse scenario (granular, 0.224 km^3; Fig. 9d) zoomed-in on Java; for clarity, 4 classes of elevations are defined as: (yellow) 0-1 m; (green) 1-2 m; (red) 2-4 m, and (pink) > 4 m. Results are compared with field measurements of flow depth and runup, from: (■) TDMRC (2019), (★) Muhari et al. (2019), (◆) Putra et al. (2020), (▼) Heidarzadeh et al. (2020), and (●) Borrero et al. (2020) surveys.

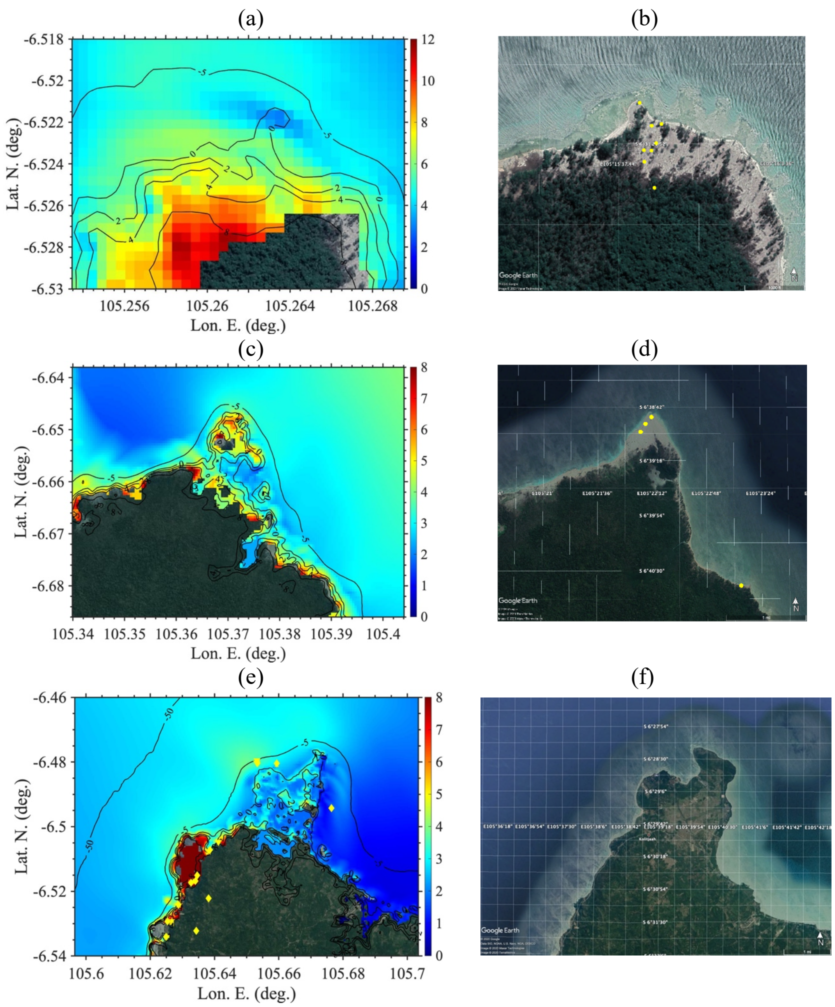

Figure 15: Maximum surface elevation (FUNWAVE, Grid G1; color scales in meter), for likeliest AK collapse scenario (granular, 0.224 km^3; Fig. 9d), zoomed on (Fig. 1a): (a) Panaitan Island (PI); (c) Ujung Kulon (UK); and (e) Kolijaah (K). (b,d,f) Google Earth image of PI, UK and K (11/20). Yellow dots in (b,d) are locations of tsunami elevation from Borrero et al.'s (2020) 02/19 survey measured from N to S, in (b) at (around Lon. E. 105.2622): 6.4, 7.3, 6.5, 6.1, 8.4, 6.4, 6, 7.4 m (MWL) (note southern point was

missing a terrain correction that was added), and in (d) at: 11.5, 11.1, 8.1, 6.9 m (MWL). Black contours in (a,c,e) are bathymetry/topography in meter and color scale is maximum surface elevation in meter.

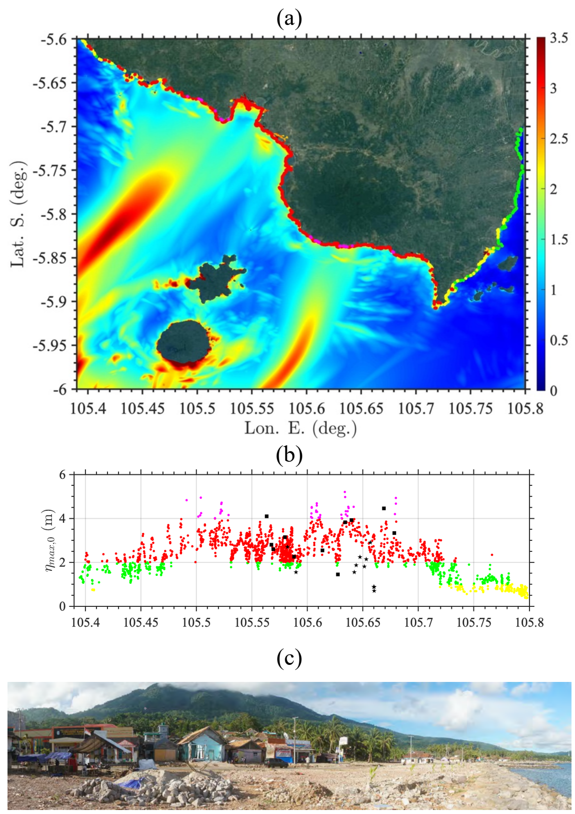

Figure 16: Same results as in Fig. 14: (a) Envelope of maximum surface elevation (FUNWAVE, Grid G1; color scales in meter), for likeliest AK collapse scenario (granular, 0.224 km^3; Fig. 9d), zoomed on Sumatra (Fig. 1); (b) comparison of computed flow depth at the shore with field surveys of: (■) TDMRC (2019), (★) Muhari et al. (2019); (c) View of Waymuli (W, Fig. 1a, 105.6348 E), looking east, from Fritz et al. (2019) 02/2019 field survey.

Supplementary file for:

Modeling of the Dec. 22nd 2018 Anak Krakatau volcano lateral collapse and tsunami based on recent field surveys: comparison with observed tsunami impact

Grilli[1] S.T., Zhang[2] C., Kirby[2] J.T., Grilli[1] A.R., Tappin[3,4] D., Watt[5] S.F.L., Hunt[6], J.E., Novellino[3], A., Engwell[3] S., Nurshal M.E.M.[7], Abdurrachman M.[7], Cassidy, M.[8], Madden-Nadeau A.L.[8] and S. Day[4]

1. Department of Ocean Engineering, University of Rhode Island, USA
2. Center for Applied Coastal Research, University of Delaware, USA
3. British Geological Survey, Nottingham, UK
4. University College, London, UK
5. School of Geography, Earth and Environmental Sciences, University of Birmingham, UK
6. National Oceanography Centre, Southampton, UK
7. Bandung Institute of Technology, Indonesia
8. Department of Earth Sciences, University of Oxford, UK

S1: Pre-and post-collapse images of Anak Krakatau

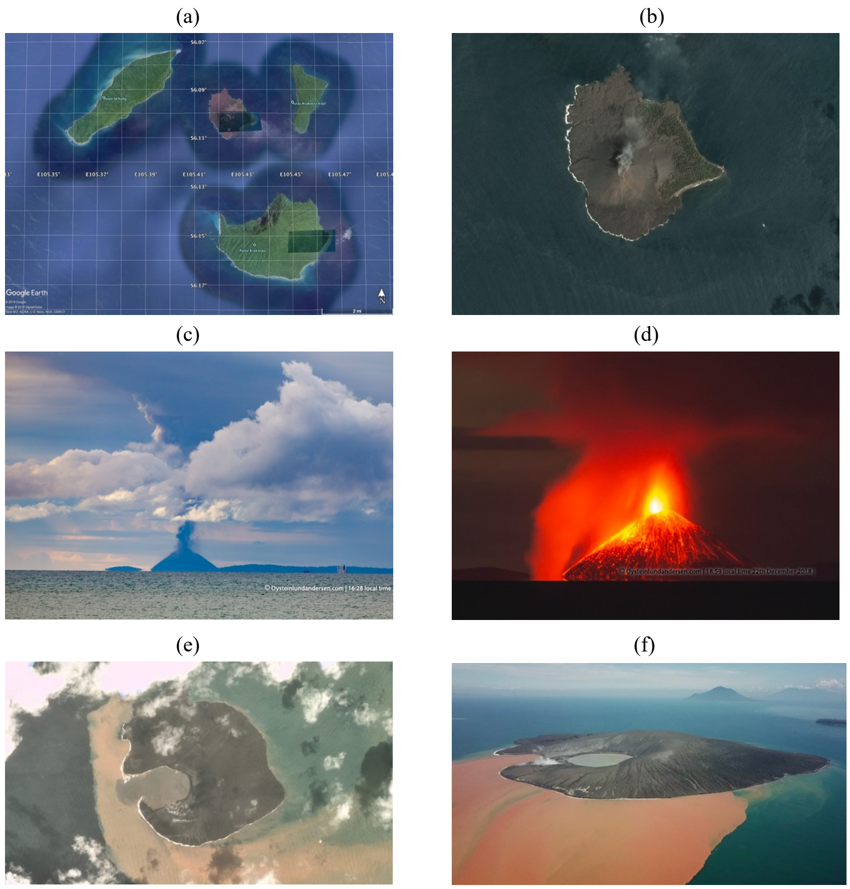

Fig. S1: (a) Pre-collapse Google Earth 2019 (DigitalGlobe Data: SIO, NOAA, U.S. Navy, NGA, GEBCO) image showing AK and Sertung (W), Panjang/Kitjil (E), and Rakata/Krakatau. (b,e) Pre- and post-AK collapse *Planet Labs* satellite images, on: (b) Dec. 17th, and (e) Dec. 30th, 2018 (AGU Blog, 2019). (c,d) Pictures taken from Java on Dec. 22, 2018 at: (c) 16:28, and (d) 18:59 local time (Andersen, 2018). (f) Jan. 11, 2019 drone survey (Reynolds, 2019).

Commented [sw20]: We could perhaps show the key satellite (CSK SAR image) and the coastline images again here, as they are important for defining the landslide margine (the same ones shown in Hunt et al.).

Commented [AN21R20]: I agree, the COSMO-SkyMed data is critical considering what we are stating in Section 3.2

S2: Non-hydrostatic versus hydrostatic NHWAVE results for near-field runups

To illustrate the effect of including the slide non-hydrostatic pressure on the flank collapse motion and generated waves, two more simulations were carried out using both viscous and granular rheology with only the hydrostatic pressure effects included within the slide layer (as in the NHWAVE version used by Grilli et al., 2019), for the collapse scenario with a 0.272 km^3 volume (Fig. 2e) identical to Grilli et al.'s (2019) preferred scenario. Results were compared with those of the same simulation performed, as in the main text, with the non-hydrostatic pressure effects included within the slide layer.

Figures S2 to S5 show instantaneous results of these simulations at different times, in vertical profiles along a 213 deg. Transect from N (Figs. S2 and S3) and in plan view (Figs. S4 and S5). In the first 20 s, for each rheology, the slide motion of the non-hydrostatic (NH) and hydrostatic (H) simulations are similar, except for a faster dynamics of the failure of the volcano summit in the H simulations.

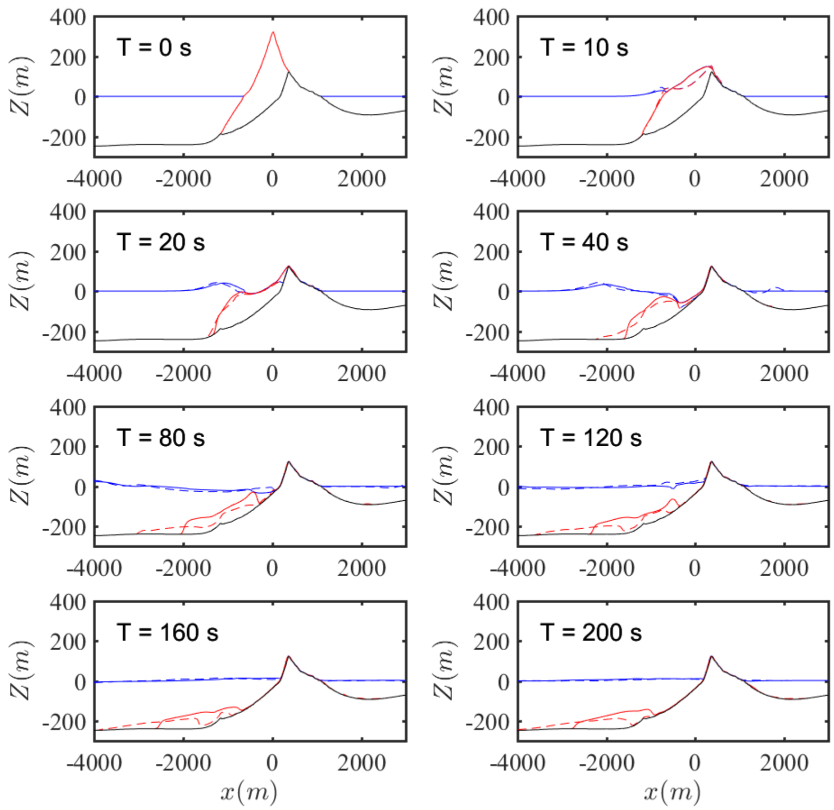

Figure S2: Grilli et al.'s likeliest AK collapse scenario (0.272 km^3) modeled with NHWAVE in Grid G2 (Fig. 1) with a granular rheology, with (solid lines) and without (dashed lines) non-hydrostatic pressure effects included within the slide layer. Sub-panels show instantaneous surface elevation (blue) and slide profiles (red), in AK transects in direction 213 deg. to north, at *t* = 0, 10, 20, 40, 80, 120, 160 and 200 s.

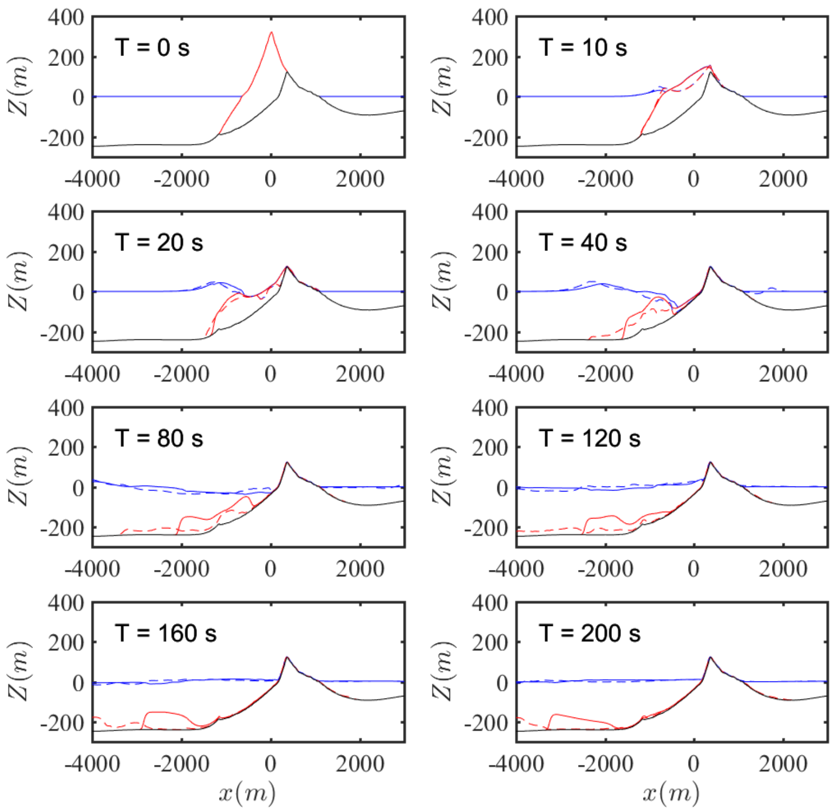

Figure S3: Same case as in Fig. S2, but for the viscous rheology.

Later in time, differences between the NH and H simulations increase as the slide tails still move at the same speed while the motion of the slide fronts are quite different, leading to a longer extent of the landslide runout and broader deposit spreading in the H simulation for both rheologies.

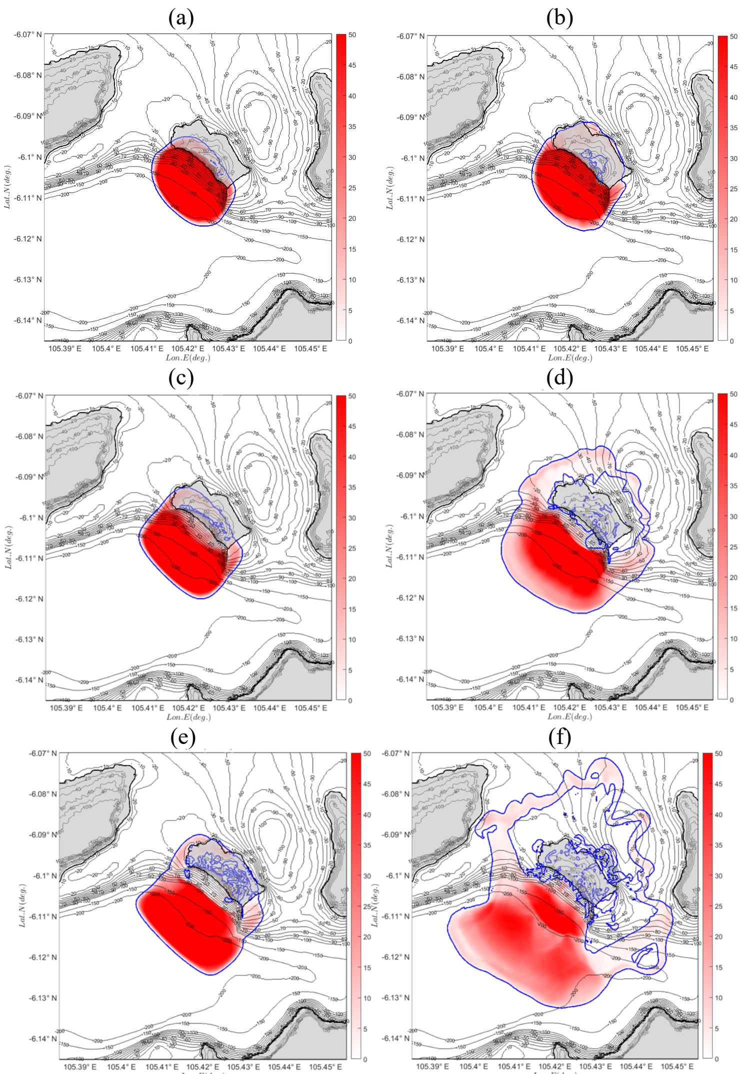

Figure S4: Results of same granular case as in Fig. S2, in plan view for (a,c,e) NH and (b,d,f) H simulations at t = (a,b) 20, (c,d) 40, and (e,f) 80 s. Solid blue line denotes slide deposit limit and color scale is slide thickness in meter.

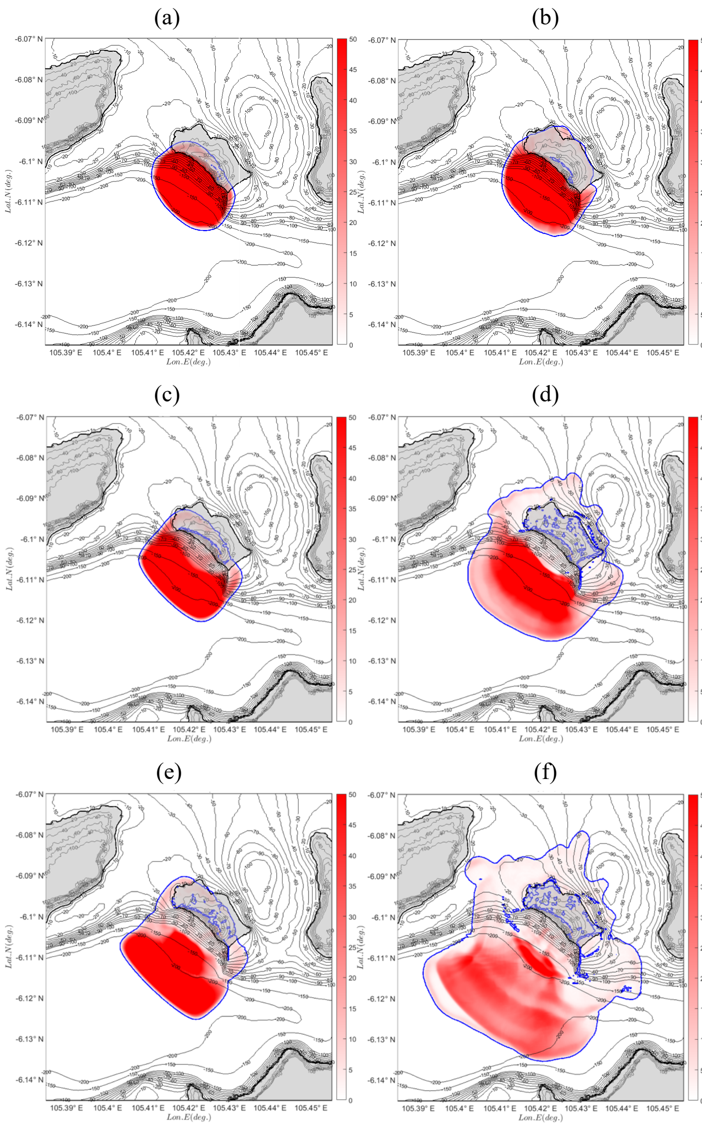

Figure S4: Results of same viscous case as in Fig. S3, in plan view for (a,c,e) NH and (b,d,f) H simulations at t = (a,b) 20, (c,d) 40, and (e,f) 80 s. Solid blue line denotes slide deposit limit and color scale is slide thickness in meter.

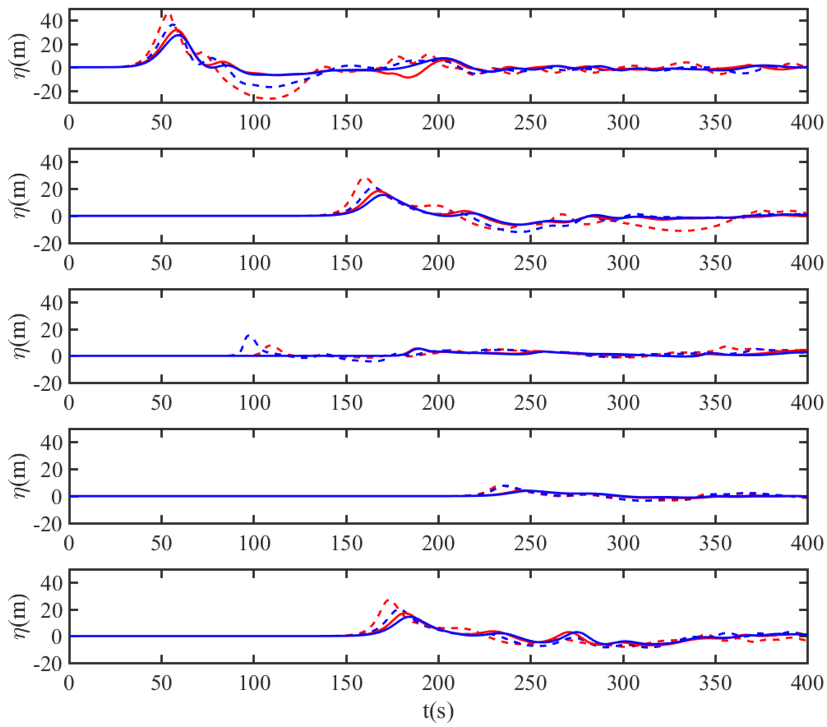

Figure S6: Results of the same granular (blue)/viscous (red) cases as in Figs. S2,S4/S3,S5. Comparison of time series of surface elevations for NH (solid) and H (dashed) simulations at numerical wave gauges (Fig. 1b), 1, 2, 5, 4, 3, from top to bottom.

For the same granular/viscous cases as shown in Figs. S2,S4/S3,S5, Figure S6 compares the time series of surface elevations computed in the NH and H simulations at numerical Wave Gauges 1 to 5 (Fig. 1b, Table 2), showing the large influence on wave generation of simulating non-hydrostatic pressures in the slide layer. Overall, while as discussed in the main text effects of rheology are only moderate on wave generation, for both rheologies, significantly larger leading waves are generated in the H simulations than

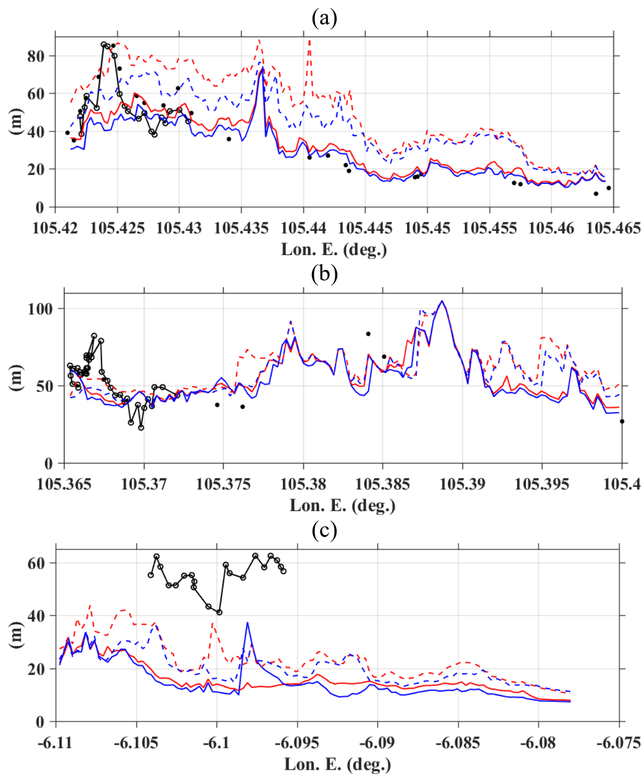

Figure S7: Results of the same granular (blue)/viscous (red) cases as in Figs. S2,S4/S3,S5. Comparison of maximum runup on AK's surrounding islands of: (a) Rakata, (b) Sertung, and (c) Panjang (Fig. 1), for NH (solid) and H (dashed) simulations. Black lines with empty circles indicate the August 2019 drone tree line survey (Fig. 11), and full circles indicate runup measured by Borrero et al. (2020) (see also Fig. 13).

in the more physically realistic NH simulations; and, in part due to amplitude dispersion effects, the waves generated in the H simulations propagate faster and arrive ahead of the waves generated in the NH simulations at all wave gauges. The same observations can be made for the first and next troughs, which are much deeper in the waves generated in the H simulations than in the NH simulations. For waves propagating to the southeast (WG 4) and northeast (WG 5), in the H simulations, there is a large leading elevation wave that is not present in the NH simulations. This appears to result from the larger slide runout occurring on the backside of AK in the H simulations (Figs. S4 and S5).

Figure S7 compares, for the same cases, the runups generated on the three surrounding islands of Rakata, Sertung and Panjang in the NH and H simulations, for both rheologies; as in Fig. 13, results are also compared to the August 2019 drone tree line survey and to runups measured by Borrero et al. (2020). The runups generated on Rakata island in the H simulations are nearly twice as large at most locations than those in the NH simulations, and show large discrepancies with the field data. The runups generated on Panjang island are also amplified in the H simulations, which is consistent with the higher waves computed at Wave Gauge 4 and 5; the H runups also significantly overestimate observations made on the north side of the island, where it was reported an 8-10 m flow depth/runup (Borrero et al., 2020). In contrast, the difference of the H and NH runups generated on Sertung island is less, except on the east side of the island where the H runups are much larger than the NH runups and again show a large discrepancy with the single runup measured in the field survey.

Based on the above, one can conclude that including non-hydrostatic effects in simulations of the slide layer motion in NHWAVE is important to accurately simulate the near-field waves and runups, as well as for simulating slide deposits and runout.